Thomas Kulterer, BSc

Investigation of Stray Paths in Fractional Horsepower Permanent-Magnet Motors

Master Thesis

Submitted in Partial Fulfillment of the Requirements for the Degree of

Diplom-Ingenieur
(Dipl.-Ing.)

in

Electrical Engineering

at

Graz University of Technology

Supervisor
Univ.-Prof. Dr.-Ing. Annette Mütze

Co-Supervisor
Dipl.-Ing. Hannes Grübler, BSc

Christian Doppler Laboratory for Brushless Drives
for Pump and Fan Applications
Electric Drives and Machines Institute
Graz University of Technology

2019

AFFIDAVIT

I declare that I have authored this thesis independently, that I have not used other than the declared sources/resources, and that I have explicitly indicated all material which has been quoted either literally or by content from the sources used. The text document uploaded to TUGRAZonline is identical to the present master thesis.

Date

Signature

Contents

Abstract

Established methods for designing electric machines are based on analytical formulas or discretized models submitted to finite element analysis. While the first variant has a short computational time it lacks a certain insight on details and the nonlinear behavior present at electric machines is not possible to cover. On the other hand, finite element analysis (FEA) provides more accurate results, but comes at the price of computational effort of several hours or days. While aforementioned motor design methodologies are well established for commercial purposes a third group is a rather new development approach, the family of approximation based models. These models need some training to work properly, but eventually provide results of good accuracy in a short time.

The goal of this master thesis is to close a gap in development of such methods by identifying the magnetic stray paths of fractional horsepower machines in their design process. With the small machines of interest here, the model development is by far not as straightforward as in the case of larger electric machines of some kilowatt rated power. For example, the properties of these small machines are significantly more subject to the influence of the manufacturing process, datasheet values do not hold any more, and 3D effects need to be considered.

The master thesis starts with comprehensive experimental investigations of an fractional horsepower example case drive, which are needed to compare the finite element analysis results realized with datasheet parameters and furthermore adapting these parameters in the finite element method (FEM) model to decreases the error between measurements and simulations. Based on the adapted FEM model the stray paths are separated and compared with simple analytical calculations to determine their error, respectively the use of these methods in fractional horsepower machines.

Zusammenfassung

Etablierte Methoden zum Entwurf elektrischer Maschinen basieren auf analytischen Formeln oder diskretisierten Modellen, die der Finite-Elemente-Analyse unterzogen werden. Während die erste Variante in Bezug auf die Rechenzeit schnell ist, fehlt ihr ein gewisser Einblick in Details, und das nichtlineare Verhalten elektrischer Maschinen ist nicht berechenbar. Auf der anderen Seite liefern Modelle, die auf der Finite-Elemente-Analyse basieren, genauere Ergebnisse, führen allerdings zu hohem Rechenaufwand von mehreren Stunden bis Tagen. Während die oben genannten Entwurfsmethoden für kommerzielle Zwecke gut etabliert sind, ist eine dritte Gruppe Gegenstand aktueller Forschung, Methoden basierend auf approximationsbasierten Modellen. Diese Modelle werden, basierend auf analytischen und numerischen Ansätzen, trainiert und liefern letztendlich Ergebnisse guter Genauigkeit in annehmbarer Zeit.

Das Ziel dieser Masterarbeit ist es, die Entwicklung solcher Methoden zu unterstützen, indem man die magnetischen Streuwege von Maschinen im Kleinleistungsbereich identifiziert, um sie im Entwurfsprozess zu berücksichtigen. Während für den Konstruktionsprozess größerer Maschinen, die insbesondere den Kleinleistungsbereich überschreiten, die Gewinnung von Konstruktionsdaten einfach ist, ist dies im unteren Leistungsbereich nicht der Fall. So sind beispielsweise die Eigenschaften dieser kleinen Maschinen deutlich stärker dem Einfluss des Herstellungsprozesses ausgesetzt, die Werte der Datenblätter halten nicht mehr, und 3D-Effekte magnetischer Streuung müssen berücksichtigt werden.

Die Masterarbeit beginnt mit umfangreichen experimentellen Untersuchungen an einem Kleinantrieb für eine Lüfteranwendung, die erforderlich sind, um die Ergebnisse der Finite-Elemente-Analyse mit Datenblattparametern zu vergleichen und diese Parameter im FEM-Modell anzupassen, um den Fehler zwischen Messungen und Simulationen zu verringern. Basierend auf dem angepassten FEM-Modell wurden die Streuwege aufgeteilt und mit analytischen Berechnungen verglichen, um deren Fehler, bzw. den Einsatz dieser Methoden für Kleinantriebe zu bestimmen.

Acknowledgement

The financial support by the Austrian Federal Ministry of Science, Research, and Economy and the National Foundation for Research, Technology, and Development is gratefully acknowledged.

This master thesis was made possible through the contribution of a number of people. I would like to thank the Electric Drives and Machines Institute at Graz University of Technology, in particular my supervisor Prof. Annette Mütze for her support. I also want to thank my co-supervisor DI Hannes Grübler for his motivation and assistance throughout the whole project.

The good cooperation with the Mechatronic Systems GmbH is appreciated.

Chapter 1

Introduction

1.1 State of the Art

Due to recent developments in the automotive industry, e.g., electrification, automated driving, or the replacement of conventional systems in cars, as well as the increasingly demanding constraints like electromagnetic compatibility (EMC), noise, vibration and harshness (NVH) or efficiency, call for an improvement of the design process of fractional horse power (FHP) drives in terms of model behavior and design time. This includes motors used in safety applications, e.g., as used in breaking systems [1], electrical drives for heat pumps in electric cars to replace the heat source compared to a internal combustion vehicle [2], all the way to fans for modern light systems [3], and oil pumps for gear boxes to increase efficiency of conventional systems [4].

The first method to design these motors is by using an analytical model. Analytical models do have the advantage to be quick in terms of computational time but lack accuracy and a certain insight into details. On the other hand a numerical approach, for example the use of finite element analysis, can be chosen. These FEM simulations come with high accuracy, but even though the computational power is continuously increasing they still need a long time for results [5,6].

The use of approximation based models (e.g., space mapping) seems to be promising but has not been established in commercially available tools yet. The space mapping method is trained by a combination of a coarse and a fine model, eventually providing results of good accuracy in a short time [7].

The goal of this master thesis is to determine the flux distribution and inductance of FHP permanent magnet machines (especially in terms of stray paths and leakage parts) with analytic calculations, compared to finite element models. The numerical investigations are supported and verified with comprehensive experimental investigations. The following sections, however, offer a general overview of small electrical drives.

1.2 Small Electric Drives

Electrical machines are often called small electrical drives or FHP machines when their power is less than 375 W [8, p. 12]. Fig. 1.1 shows the application areas of small electrical drives (used as auxiliary drives) in a car. About 50 - 100 small motors are used for different applications in a compact car. More than 76 % are used for comfort-related drives, for example window lifters, seat adjustment and central locking systems. 17 % are used in basic auxiliary drives such as fuel, water and oil pumps and about 7 % for safety applications, including anti-lock braking system and windscreen wipers [9, p. 5-9]. Generally, permanent magnet machines are used for these applications [10, p. 6-7].

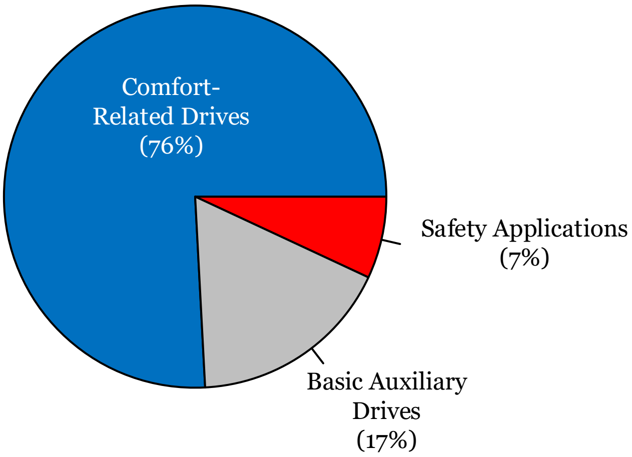

Figure 1.1: Application area of electrical machines used as auxiliary drives in a car from [9, p. 5-9].

1.3 Introduction to Small BLDC Machines

Most of the motors used in cars are permanent magnet electric motors. They provide a high energy density which results in small size machine designs. Many of them are using brushless (electrical) commutation instead of mechanical brushes and commutators. These machines can generally be separated into two types of motors [11]:

- Brushless DC Motors (BLDC)
- Permanent Magnet Synchronous Motors (PMSM)

These two machines differ by their commutation. While PMSM are sine commuted and need closed loop control, BLDC motors normally do have block commutation, often realized with a simple open loop control. This determines the price. Another difference between PMSM and BLDC machines is the back-electromotive force or BEMF (u_{EMF}). Different magnetization of the magnets lead to either a sine wave BEMF, respectively to a trapezoid-shaped BEMF [11].

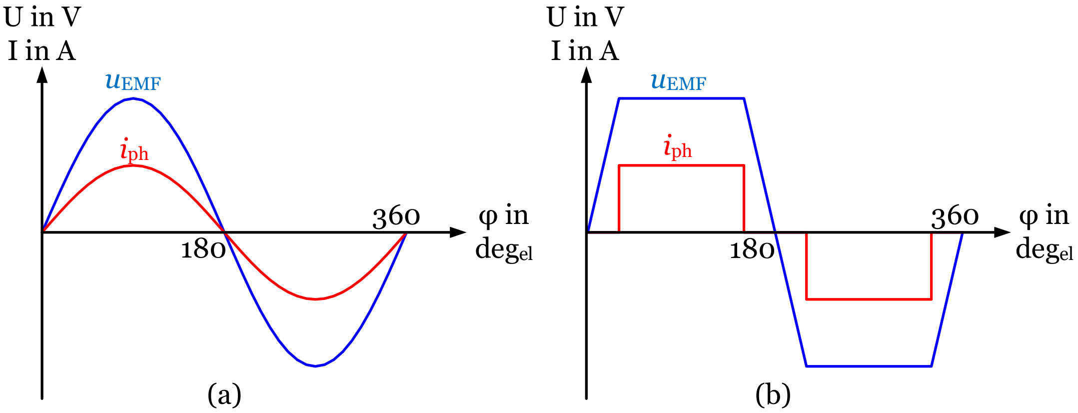

Figure 1.2: BEMF and phase current (a) for BLAC machines and (b) for BLDC machines [11].

Fig. 1.2(a) and Fig. 1.2(b) show the BEMF and the phase current of one phase of the PMSM (often used with sine wave BEMF), and an BLDC motor, respectively (usually operating with trapezoid-shaped BEMF). Advantages of BLDC motors are lower switching losses and lower costs. On the other hand, the BLDC machines produce higher torque ripple during commutation and therefore more noise (NVH), together with higher core losses, due to higher harmonics [12].

Electric machines in general, and hence BLDC machines can be further divided by the position or placement of the rotor and the stator [13, p. 117-124]:

- Inner-Rotor Motors
- Outer-Rotor Motors
- Pancake Motors
- Linear Motors

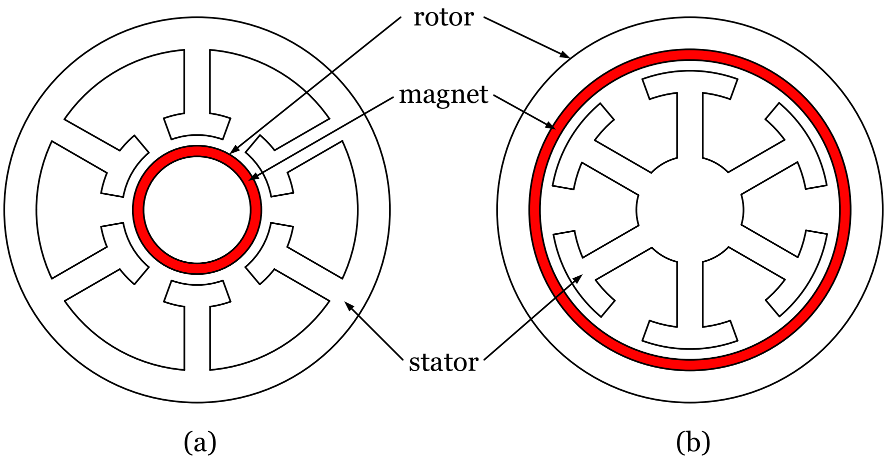

Figure 1.3: Illustration of (a) inner-rotor and (b) outer-rotor motors [13, p. 117-121].

Fig. 1.3(a) and Fig. 1.3(b) show the illustration of inner-rotor and outer-rotor machines (often called inside out motors) respectively. These two motor types differ in their fields of application. Inner-rotor-type motors are often used in highly dynamic applications, because of the lower inertia torque. Another advantage is that the windings are on the outside (better heat emission). In contrast to this, outer-rotor motors have easier winding assemblies and a larger air gap radius, which leads to higher torque. Another advantage of these machines is that e.g., fan blades can be directly attached to the rotor and hence they are often used in pumps, fans and hard disc drives [13, p. 117-124].

Furthermore, machines can be distinguished by their number of phases, namely multi-phase and single-phase machines. Most multi-phase machines are designed as three phase machines as shown in Fig. 1.4(a). Because of their higher efficiency (always two phases are energized) they are commonly used in applications where more power is needed. Another aspect is that the return conductor can be omitted. Such machines normally need six switches for their control. The electric circuit is illustrated in Fig. 1.5.

Due to limited space in small electric drives, single-phase machines are typically used for powers of a few watts, see Fig. 1.4(b). Although they are less efficient

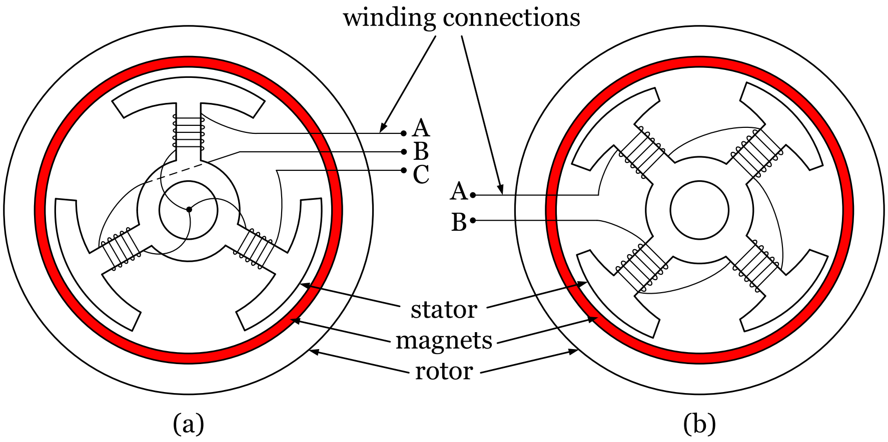

Figure 1.4: Model of (a) a 3-phase motor adapted from [14] and (b) a 1-phase motor design from [15].

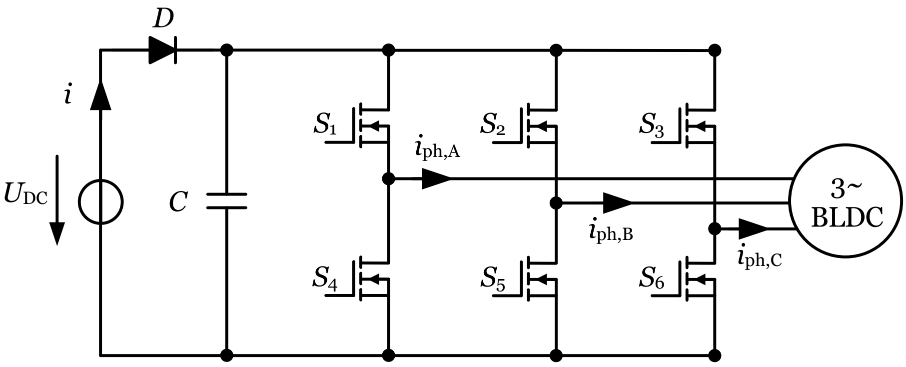

Figure 1.5: Electric circuit for the three phase machine from [16].

than three phase motors their advantages are that they are less costly and easier to manufacture [17]. Single-phase brushless DC motors are often used in applications where low starting torque is needed, e.g., pumps or fans. These motors have the disadvantage that they have a position with zero torque (also called dead points) which can lead to problems at the start of the motor. Therefore, these machines need an asymmetrical air gap to create an additional reluctance torque component. This can be realized with a tapered-air gap, with stepped-teeth, with asymmetric-teeth, or with notched-teeth [18]. As per [19], a tapered-air gap is best in terms of cogging torque peaks. Another method for a self-starting rotor position could be achieved with parking magnets. This has the disadvantage of more costs for the motor and is hence not often used with small machines [20].

Single-phase machines can be separated in monofilar wound motors or bifilar wound motors as illustrated in Fig. 1.6(a) and Fig. 1.6(b). Monofilar wound machines just have one wire, which is wound alternating around the stator teeth. In contrast, bifilar wound motors have two coils wound around each tooth in alternating directions. Here, one end of one coil is connected to the end of the other coil and the winding terminals are connected separately. The electric circuits of a monofilar wound machine and of a bifilar wound machine are shown in Fig. 1.7 and Fig. 1.8. The BLDC motor is represented as a serial connection from an inductance, a resistor

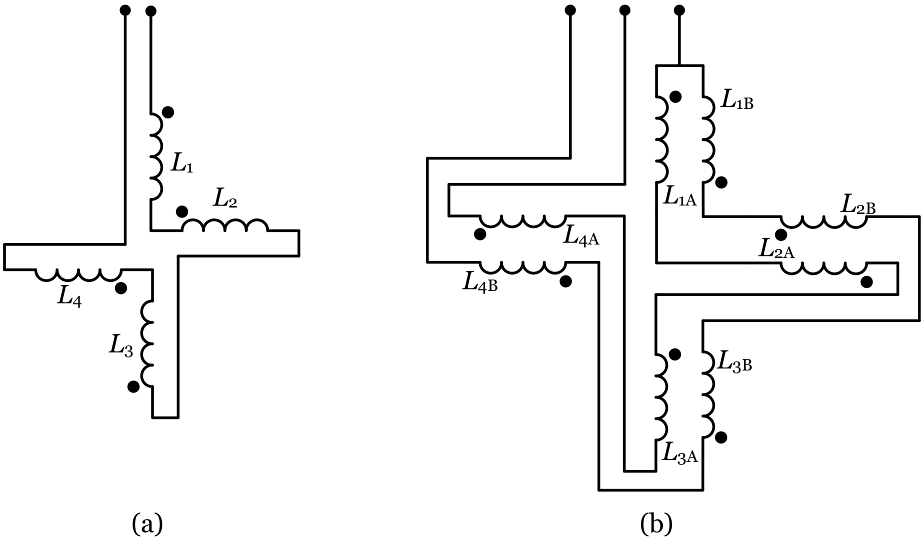

Figure 1.6: Winding configuration (a) monofilar winding from [21] and (b) bifilar winding from [7].

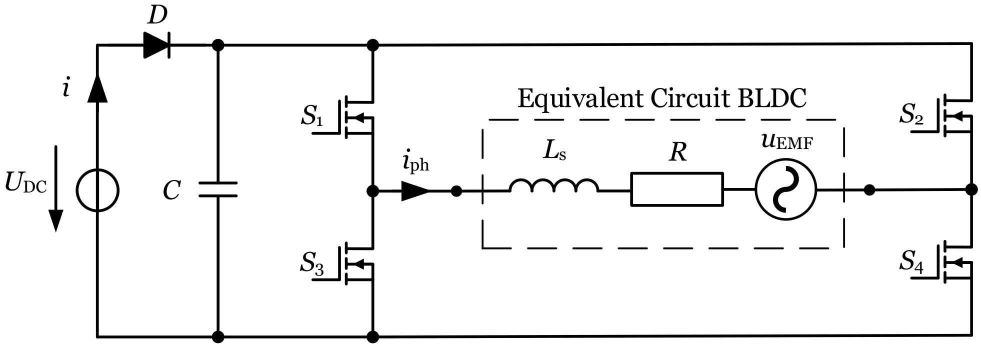

Figure 1.7: Electric circuit for monofilar winding from [22].

and the BEMF-source. Machines with monofilar windings need four switches to run the motor. Although bifilar wound motors need more copper than monofilar wound machines, they only require two switches. Hence, bifilar wound machines are more common in low budget drives. Recent trends of integrating power electronics and logic to a system on chip may bring a shift in selection of motor topologies [24].

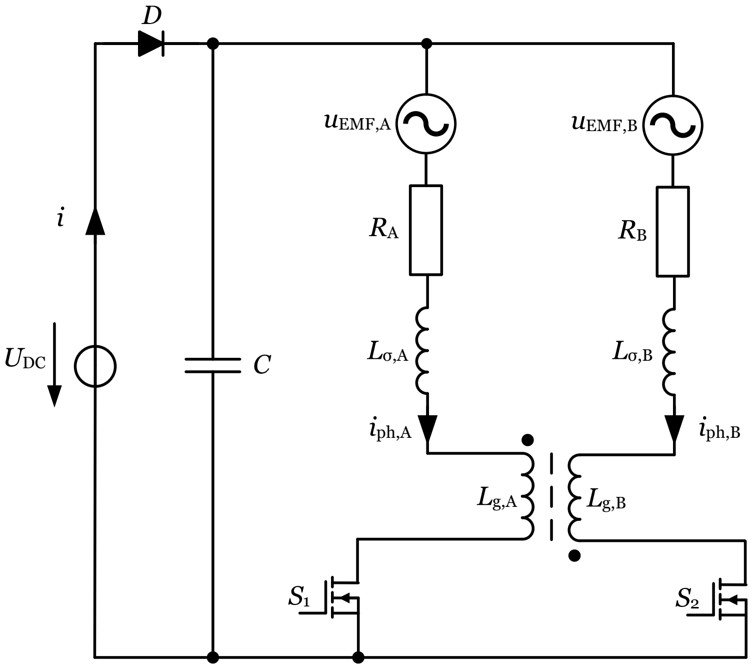

Figure 1.8: Electric circuit for bifilar winding from [23].

1.4 Structure of the Master Thesis

The following Chapter is concerned with the introduction of the example case drive used for the investigations. Then, the stray paths investigation is separated into two topics, permanent magnet excited and current excited flux, are discussed.

First, the open circuit investigations, which are concerned with stray paths of permanent magnet excited magnetic flux. These stray paths mainly affect the BEMF. Therefore, Chapter 3 is concerned with experimental investigations of the example case drive, as well as the adaptation of the parameters used for the 3D-FEM motor model. Then, the stray paths for this case have been separated using the 3D-FEM simulation results. Chapter 4 analyses the 2D stray paths of the example case machine. Again, the stray paths have been separated with the use of a 2D-FEM model, with the adapted parameters. Then 2D analytic calculations, using simple magnetic equivalent circuits (MECs) have been developed and added for different leakage parts. The results of these MECs have been compared to the 2D-FEM simulation results to evaluate accuracy. In Chapter 5, the MEC of the 2D case has been extended by the 3D stray paths and, again, have been compared to the FEM simulation results (now to the adapted 3D-FEM model) to show the accuracy of the analytic calculations.

The second investigation is concerned with stray paths of current excited magnetic flux (leakage inductances). Again, experimental investigations of the example case machine to determine the inductances have been realized (Chapter 6). Next, the 3D-FEM parameters have been adapted step by step and the improvement of the simulated results have been compared to the measured values. After that, the inductance of the motor has been separated with the use of FEM simulations. In Chapter 7 the inductances have been determined with analytic calculations and have been compared to the separated inductances from the FEM simulated results.

Chapter 2

Introduction of the Example Case Drive

2.1 Single Phase Fan Application

This master thesis investigates a four-pole single-phase brushless DC (inside out) motor as used in a fan system. These are the most popular designs for small electric drives used in, e.g., the automotive industry for small fans and pumps. The example case machine has a bonded magnetic ring, an asymmetric air gap, a bifilar winding and a rotor overhang. The nominal speed of the motor is 5000 rpm. The example case drive can operate in a voltage range from 8 V to 16 V.

2.2 Permanent Magnets and Their Magnetization

The four-pole machine uses NeFeB magnets, a rare earth material with high residual flux densities and no breaking point (or knee) in the *BH*-curve [25, p. 144-147]. Fig. 2.1(b) shows the datasheet values for the residual flux density B_r and the coercive field strength H_c at three different temperatures. The demagnetization curves (*BH*-curves) of the magnetic ring for these temperatures are shown in Fig. 2.1(a).

The magnetic ring of the machine has a radial magnetization with linear rising and falling transition zones, which means that the residual flux density is constant in the middle of one pole (θ_mag) and decreases linearly leaving the center (θ_fall and θ_rise), see Fig. 2.2(a).

For facilitating analytic calculations, piecewise linearization is introduced. The mean value of the magnetic flux density of one pole (with the angle θ_p) can then be

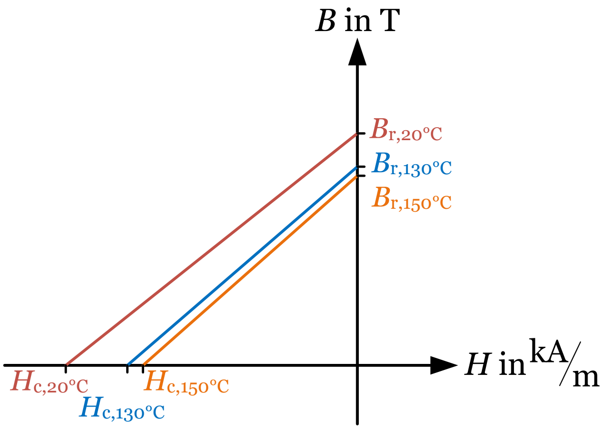

(a)

Parameters of the Used Magnets		
Temperature	B_r	H_c
20 °C	460 mT	289.3 kA/m
130 °C	394 mT	228.2 kA/m
150 °C	376 mT	212.7 kA/m

(b)

Figure 2.1: Datasheet parameters (a) as *BH*-curve diagram and (b) as table with values at different temperatures.

calculated with (2.1). This mean value can then be used to calculate an equivalent rectangular magnet, as shown in Fig.2.2(b), where θ_{mg} and θ_{ms} are the zones with constant magnetization and zero magnetization, respectively.

$$\frac{1}{\theta_{\mathrm{p}}}\int_{0}^{\theta_{\mathrm{p}}} B_{\mathrm{r}} d\theta = \frac{1}{\theta_{\mathrm{p}}}\left[\int_{\theta_{\mathrm{rise}}} \frac{B_{\mathrm{r}}}{\theta_{\mathrm{rise}}}\theta d\theta \int_{\theta_{\mathrm{mag}}} B_{\mathrm{r}} d\theta \int_{\theta_{\mathrm{fall}}} \left(\frac{-B_{\mathrm{r}}}{\theta_{\mathrm{fall}}}\theta + B_{\mathrm{r}}\right) d\theta\right] \tag{2.1}$$

The magnetizations (flux density of one pole) of both magnets are shown in Fig. 2.3. When the rising and falling angles of the magnetic ring are equal ($\theta_{\mathrm{rise}} = \theta_{\mathrm{fall}}$) and linear, the boundaries of the equivalent rectangular magnets are given by:

$$\theta_{\mathrm{mg}} = \theta_{\mathrm{mag}} + \theta_{\mathrm{rise}} \quad \text{and} \quad \theta_{\mathrm{ms}} = \theta_{\mathrm{fall}} \tag{2.2}$$

Fig. 2.3(a) and Fig. 2.3(b) shows the flux distributions of the magnetic ring, respectively the equivalent rectangular magnets,resulting in the same flux per pole.

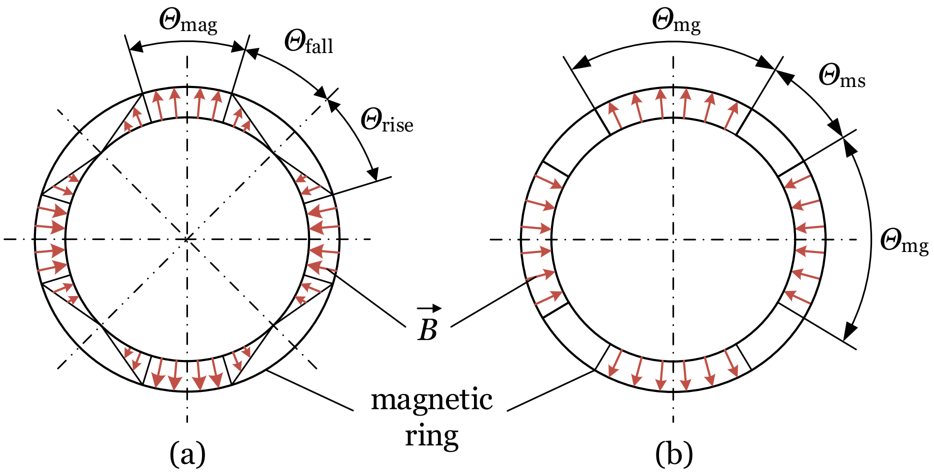

Figure 2.2: Magnetization of (a) the magnetic ring and (b) the equivalent rectangular magnets.

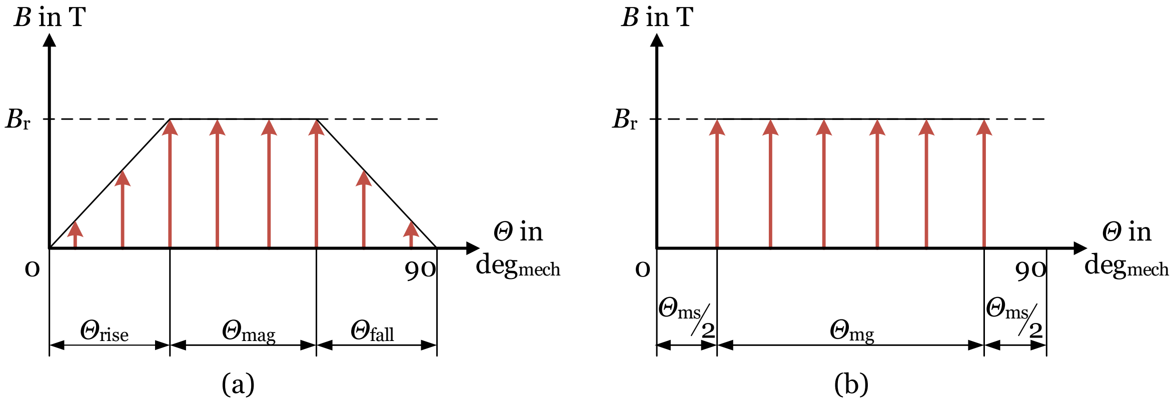

Figure 2.3: Flux distribution of one pole from (a) the magnetic ring and (b) the equivalent rectangular magnets.

2.3 Rotor and Stator

The stator of the example case motor is made of laminated electrical sheets. It is manufactured and assembled from individual punched parts connected with interlockings. The geometry of a single stator sheet is shown in Fig. 2.4(a). The rotor consists of the rotor back iron (made of machining steel) and the bonded permanent magnetic ring, see Fig. 2.4(b).

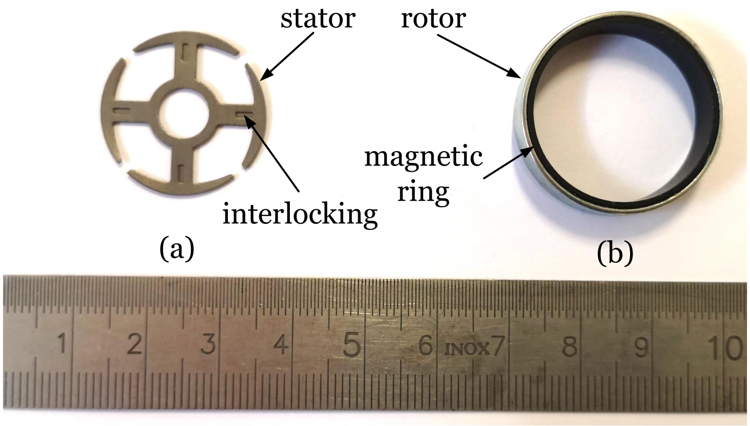

Figure 2.4: Geometries of (a) the stator iron and (b) the rotor.

2.4 Machine Dimensions

A sketch of the investigated machine is shown in Fig. 2.5(a). The dimensions of the machine are shown in Tab. 2.1. Because of the circular construction of the motor the mean values of the circular distances are used. For facilitating analytic calculations, the mean air gap radius is used and the asymmetric air gap has been neglected.

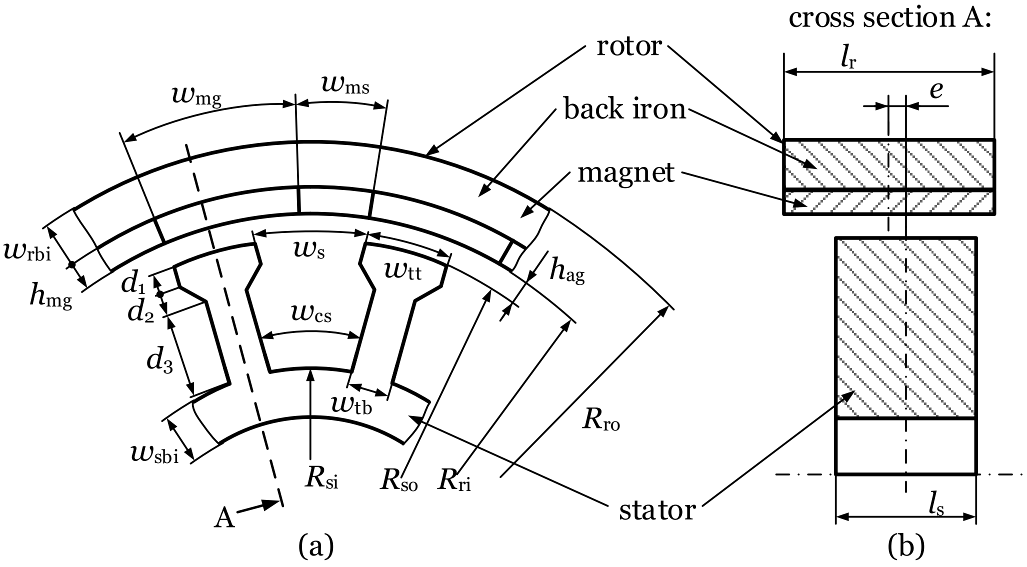

Figure 2.5: Geometry and dimensions (a) of the BLDC motor (modified form [26]) and (b) the cross sectional view.

Fig. 2.5(b) shows the axial dimensions of the machine with rotor overhang and axial offset. Rotor overhang is mostly used in motors with weak magnetic material to increase the magnetic flux in the stator [27, p. 95]. Furthermore, the axial displacement between the rotor and the stator leads to an axial force which can be used to fix the rotor shaft safely with magnetic pull.

The values from Tab. 2.1 have been used for the calculations, where A_{m} is the cross sectional area of the magnet ($w_{\mathrm{mg}} \cdot l_{\mathrm{r}}$) and A_{g} is the air gap cross section. The distance w_{cs}, as it is typically defined in the literature, is calculated at one third of the stator tooth height and the distance d_2 of the example case machine is zero.

Dimensions of the Example Case Machine in mm					
Outer Rotor Radius	R_{ro}	13.75	Inner Rotor Radius	R_{ri}	12
Outer Stator Radius	R_{so}	11.5	Inner Stator Radius	R_{si}	5
Rotor Yoke Height	w_{rbi}	0.975	Magnet Height	h_{mg}	0.775
Air Gap Height	h_{ag}	0.5	Stator Tooth Tip Height	d_1	1.7
Stator Tooth Height	d_3	4.8	Stator Yoke Height	w_{sbi}	1.5
Rotor Yoke Width	w_{ry}	20.8	Magnet Width	w_{mg}	13.4
Magnet to Magnet Width	w_{ms}	6.1	Stator Tooth Tip Width	w_{tt}	16.6
Stator Tooth Width	w_{tb}	3	Stator Yoke Width	w_{sy}	6.7
Tooth Tip to Tooth Tip Width	w_{s}	1.45	Tooth to Tooth Width	w_{cs}	8.6
Stator Length	l_{s}	4.2	Rotor Length	l_{r}	6

Table 2.1: Dimensions of the machine used for the investigations from Fig. 2.5.

Chapter 3

Experimental Investigation and FEM Model Adaptation

This Chapters aim is to determine the stray paths that affect the flux of the PM with open circuit investigations. First, experimental investigations of the example case drive have been realized, performing measurements of the BEMF, the magnetization of the rotor (including rotor back iron and magnetic ring) and the magnetic parameters of the stator and rotor back iron. Next, the results of the measurements have been compared to the 3D-FEM simulation results, performed with datasheet values. By adapting the parameters of the FEM model the error between the experimental investigations and FEM simulations has been reduced. Then, the adapted FEM model has been used to separate the stray paths of the example case drive.

3.1 Experimental Setup

For the experimental investigations of the machine, a motor test bench as shown in Fig. 3.1 has been used. This motor test bench consists of a servo motor (II) which is fitted on a mounting bracket. This servo motor can be operated with speed, position and torque control. The rotor (III) can be directly attached to the servo motor while the stator (IV) is mounted on a holding device. For the measurements a data recorder (I) from HBM [28] has been used, which provides high accuracy. Also the coil current of the stator has been measured with the use of a current sensor (V) from [29].
Then the measured results are compared to the simulated 3D-FEM results from JMAG [30]. The data evaluation was carried out with MATLAB/Simulink [31].

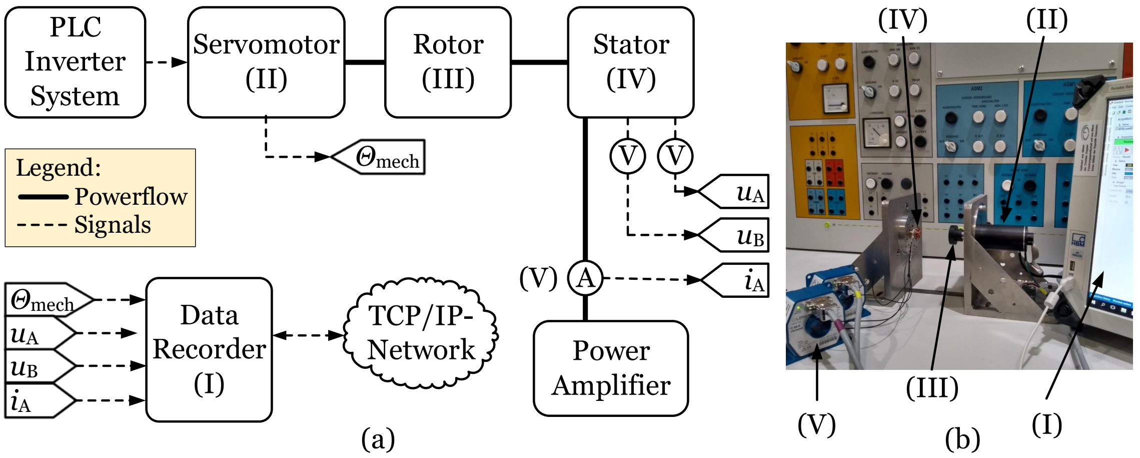

Figure 3.1: Motor test bench, (a) block diagram and (b) a picture of the setup.

3.2 Measurement of the BEMF

To measure the BEMF of the example case motor, the experimental setup from Chapter 3.1 has been used, where the rotor has been attached to the servo motor and the stator has been mounted onto the holding device. After the stator and the rotor position have been adjusted, the BEMF of both phases have been measured at a rotating speed of 5000 rpm and have been compared to the 3D-FEM simulated results (with datasheet values), see Fig. 3.2. The amplitude of the simulated BEMF is

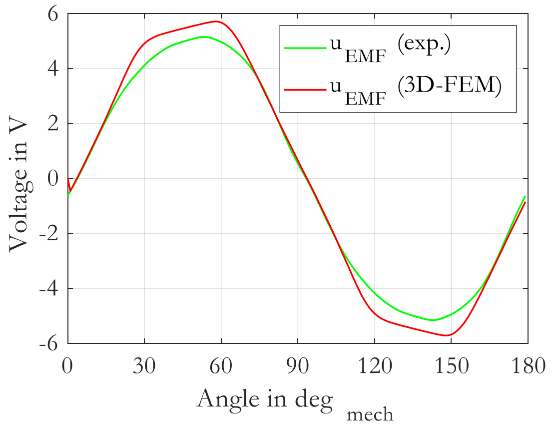

Figure 3.2: BEMF of 3D-FEM and the experimental case machine.

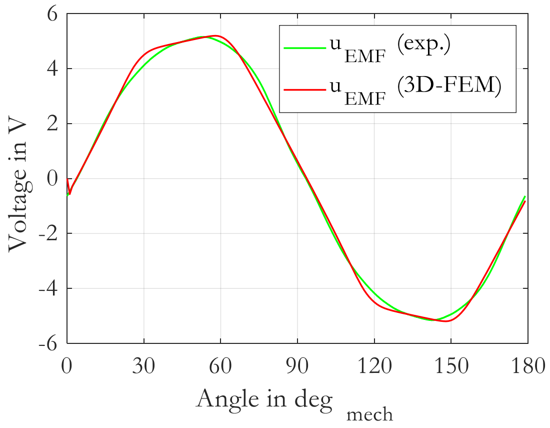

Figure 3.3: BEMF of 3D-FEM with reduced B_{r} and H_{c}.

larger than the measured one. This has been corrected by reducing the residual flux density (B_r) and coercive field strength (H_c) of the magnetic ring. With the adapted magnet parameters the simulation has been performed again, see Fig. 3.3. While the amplitudes of the BEMF of the simulated and measured motor agree well, their waveforms still differ. Therefore, further investigations on the magnetization of the magnetic ring seemed to be necessary and are discussed in the next section.

3.3 Investigation of the Magnetic Ring with Magnetic Field Measurements

Since the waveform of the simulated BEMF did not agree well with the measured one, the magnetic ring magnetization was investigated. To this aim, a slightly different motor test bench setup was used. The rotor with the magnetic ring and the back iron were mounted on the testing device, as before. The stator has been replaced by a Hall sensor bracket (see Fig. 3.4), which contains two grooves to hold two Hall sensors from [32], to measure the magnetic flux density. It is made of plastic so that the material does not influence the magnetic flux. The Hall sensors are placed at the top and on the bottom of the Hall bracket, to consider tolerances of the arrangement. Then, the magnetic flux density in the axial center of the rotor has been measured for a given rotating speed. According to the datasheet, the magnetic ring of the

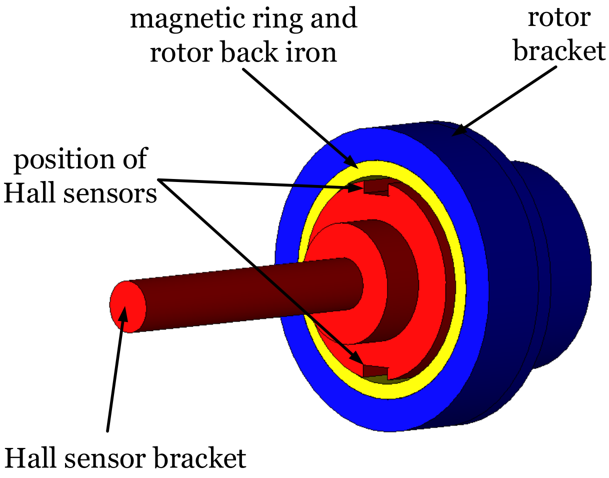

Figure 3.4: 3D-CAD model of the Hall sensor bracket and the rotor.

example case drive has a radial magnetization pattern with linear transition zones (see Fig. 3.5(a)). Fig. 3.6 shows the measured flux density of the experimental case drive and the simulated flux density from 3D-FEM on the same position as the Hall sensor bracket. While the amplitude of both flux densities agree well, their waveforms differ.

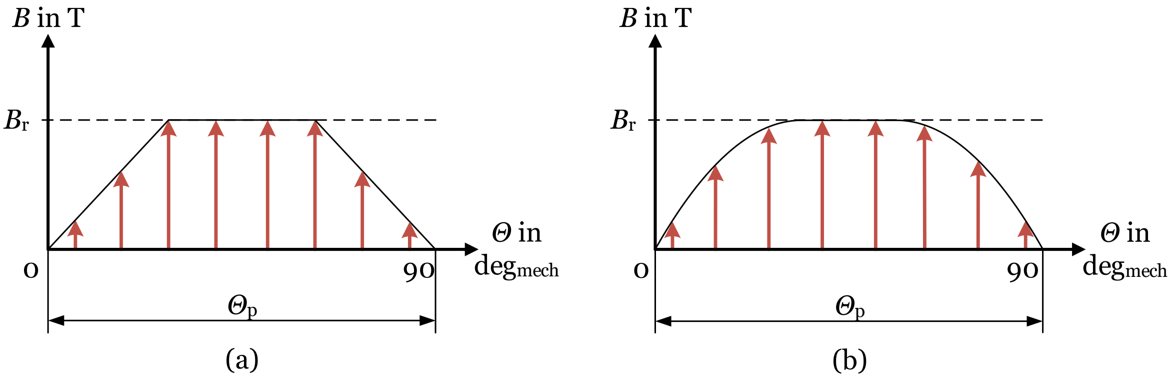

Figure 3.5: Magnetization of one pole (θ_p) of the magnetic ring with (a) linear transition zones and (b) parabolic transition zones.

Fig. 3.5(b) shows the adapted magnetization of the magnetic ring (including radial magnetization pattern with parabolic transition zones), used for the new 3D-FEM simulation. Fig. 3.7 shows the 3D-FEM simulation result with adapted magnetiza-

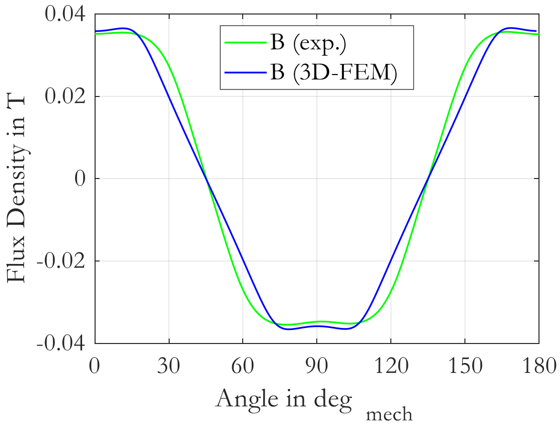

Figure 3.6: Measured and simulated 3D-FEM flux density with linear transition zones.

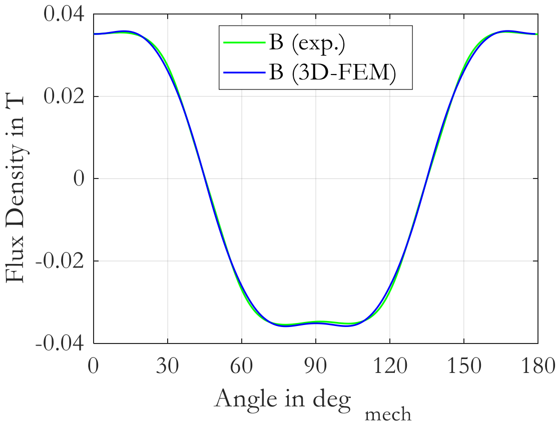

Figure 3.7: Measured and simulated 3D-FEM flux density with adapted parabolic transition zones.

tion, again, compared to the measured result. Now, the amplitudes of both flux densities, as well as their waveforms agree well.

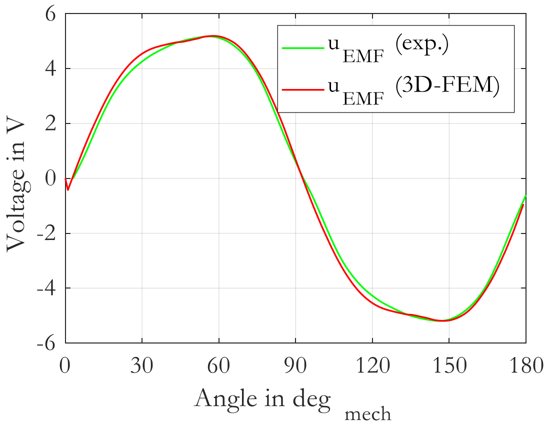

Figure 3.8: BEMF with modified 3D-FEM magnetization from Fig. 3.5(b).

Using the adapted magnetization of the magnetic ring, the 3D-FEM simulation for the BEMF has been repeated and compared to the measured voltage, see Fig. 3.8. As expected (from Faraday's law of induction), the amplitude and the waveform of the simulated and measured BEMF agree well now.

3.4 Investigation of the Soft Magnetic Material Properties

Next, the soft magnetic properties of the rotor and stator steel material were investigated. Manufacturing processes, such as laser cutting, mechanical cutting and punching, on electrical steel can have big influence in terms of their magnetization characteristics [33–35]. Therefore, the magnetic properties of the stator iron and rotor back iron have been investigated with an AC-test, respectively a DC-test. The experimental investigations are explained in the Appendix A.1.

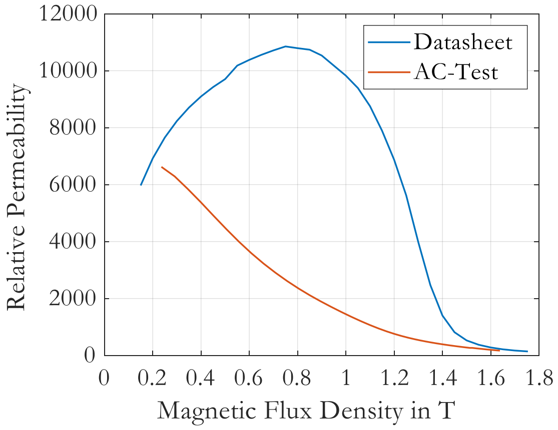

Figure 3.9: $\mu_\mathrm{r}B$-curves of stator iron, datasheet versus measurement.

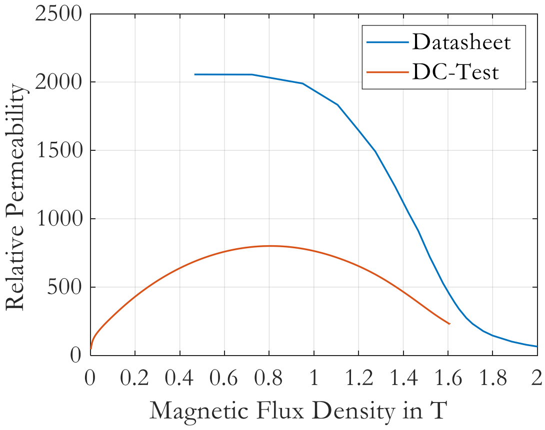

Figure 3.10: $\mu_\mathrm{r}B$-curves of rotor back iron, datasheet versus measurement.

Fig. 3.9 and Fig. 3.10 show the $\mu_\mathrm{r}B$-curves for the datasheet values compared to the measured results for the stator steel and the rotor steel, respectively. The influence due to manufacturing processes is enormous and decreases the magnetic properties compared to the datasheet parameters. With the results of the measured rotor and stator steel parameters, the 3D-FEM simulation has been repeated and compared to the measured BEMF of the example case drive. Due to the influence of the adapted steel the amplitude of the BEMF has slightly decreased but still agrees well compared to the measured BEMF.

3.5 Stray Path Allocation for the Open Circuit

Since the 3D-FEM model of the machine has been adapted, now the stray paths have been allocated using 3D-FEM. Since the magnetic flux distribution of the machine and so the stray paths vary in every position, the 3D-FEM model has been investigated in the position where the magnet is directly above the stator tooth (at 0 $\mathrm{deg_{mech}}$ as illustrated in Fig. 3.11(b)). This position has most influence on the slope of the stator flux (see Fig.3.12 at 0 $\mathrm{deg_{mech}}$), which determines the BEMF; and also the following analytic calculations have been performed in this position.
Then, the leakage fluxes have been located, using the 3D-FEM simulation results. The leakage terms have been separated into a stator leakage flux and a rotor leakage flux, as shown in the flow chart in Fig. 3.11(a). The magnet flux (the flux which is leaving the magnet, ϕ_m) can be separated in the air gap flux ϕ_g (crossing the air gap) and the rotor leakage flux (ϕ_rl, which closes from the magnet directly to the rotor, respectively to the other magnet). Furthermore, the air gap flux can be separated in the stator leakage flux (ϕ_sl, from stator tooth tip to stator tooth tip and across the slots) and the stator iron flux ϕ_s (respectively stator linkage flux). The stator iron flux is the part of the flux which causes the BEMF of the machine. Tab. 3.1 shows the results for the stray paths separation of the machine. The largest leakage part

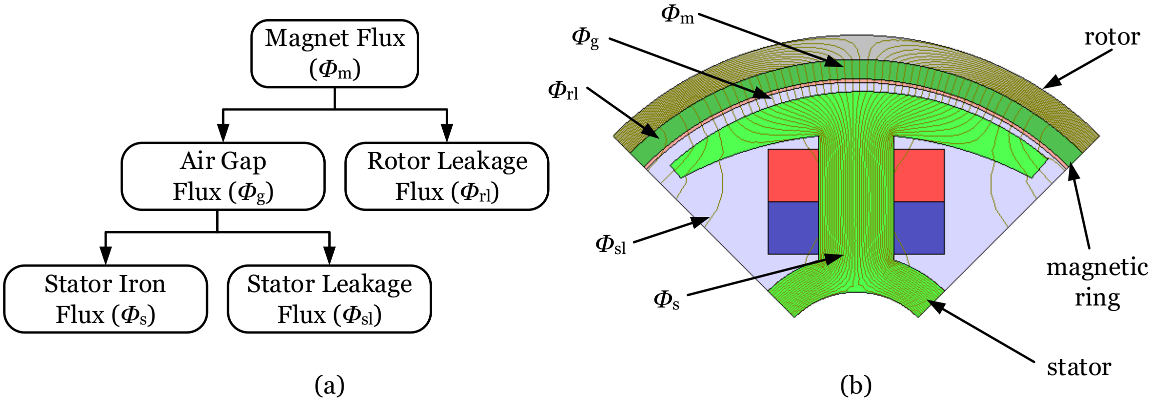

Figure 3.11: Separated flux terms of the machine illustrated as (a) flow chart and (b) magnetic flux lines from the FEM model.

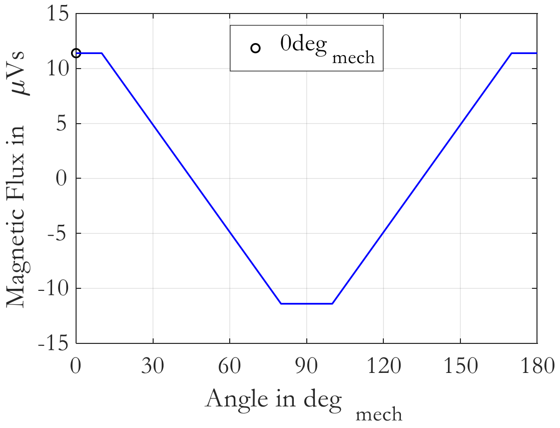

Figure 3.12: Ideal stator iron flux with illustrated position for stray paths separation.

Flux Part	Symbol	Value	Percent of Total
Magnet Flux	ϕ_m	15.53μVs	100%
Rotor Leakage Flux	ϕ_{rl}	1.54μVs	9.9%
Air Gap Flux	ϕ_g	13.99μVs	90.1%
Stator Leakage Flux	ϕ_{sl}	0.12μVs	0.8%
Stator Iron Flux	ϕ_s	13.87μVs	89.3%

Table 3.1: Separated flux paths of the example case machine determined with 3D-FEM simulation results.

appears in the rotor. On the other hand, the leakage of the stator is small compared to the one occurring in the rotor. This may be attributed to the high saturation of the rotor back iron resulting in low permeability of the rotor steel, as well as the rotor overhang. This leads to a total flux leakage factor (from [36], using the stator iron flux instead of the air gap flux, which basically describes the ratio of the linkage flux to the total flux in per unit) of about 0.9.

Chapter 4

Calculation of Stray Paths Using a Magnetic Equivalent Circuit Model

This Chapter analyses the use of a magnetic equivalent circuit for analytic calculation of FHP BLDC machines. First, the 2D case has been calculated, neglecting 3D effects such as the rotor overhang. To evaluate and compare the analytic calculations a 2D-FEM model with the adapted parameters has been developed. Then, a 2D-MEC has been implemented and extended (subsequently) with the different leakage terms and the rotor and stator steel parameters. Every MEC extension step has been compared to the adapted 2D-FEM simulation results to determine the impact and error of each step. The goal is to determine the use, respectively the error of basic analytic models and equations. Therefore, a symmetrical analytic model has been created, neglecting the asymmetric air gap. The magnetic ring has been simplified for the analytic calculations as well (see Chapter 2.2).

4.1 2D-FEM Simulation Results

First, a 2D-FEM model of the example case drive, with the adapted parameters form the previous Chapter has been created. The 2D-FEM model neglects the rotor overhang (so rotor and stator have the same axial lengths) and the three dimensional stray paths on the end face of the rotor and stator. Then, the magnetic fluxes have been separated using the 2D-FEM model, to evaluate the analytic calculations with the use of the MEC. Tab. 4.1 shows the results of the flux paths and their percentage of total flux of the FEM simulation. Compared to the 3D-FEM simulation results from the previous Chapter, the leakage flux factor of the 2D-FEM is 0.97, respectively

Flux Part	Symbol	Value	Percent of Total
Magnet Flux	ϕ_m	11.84 μVs	100 %
Rotor Leakage Flux	ϕ_rl	0.27 μVs	2.3 %
Air Gap Flux	ϕ_g	11.57 μVs	97.7 %
Stator Leakage Flux	ϕ_sl	0.08 μVs	0.7 %
Stator Linkage Flux	ϕ_s	11.49 μVs	97 %

Table 4.1: Magnetic flux separation determined by 2D-FEM simulation with adjusted parameters.

the leakage is just 3 %. Again, more leakage occurs in the rotor. But on the other hand, the stator iron flux is decreased by about 20 %, due to the missing magnet area from the rotor overhang. The following analytic calculation results for the 2D case have been compared to these values.

4.2 Magnetic Circuit Calculated with a Leakage Factor

The first calculation methods for the design step for large machines (especially leaving the FHP range) is by using leakage factors for the analytic calculations [13, p. 68-72]. Therefore, a simple model of the machine is used where every path that the magnetic flux will pass is represented by a magnetic resistance (reluctance), see Fig. 4.1. The magnets are represented as flux sources with internal reluctances. In this case, the armature reaction, the saturation, and the non-linearity are neglected and the simplified model just considers the reluctance of the air gap and the internal magnet reluctance. Then, a leakage factor (K_l) and a reluctance factor (K_r) to consider the leakage flux and the stator and rotor iron, respectively were introduced. The flux leaving the magnet (4.1) and the air gap flux (4.2) are calculated by:

$$\phi_\mathrm{m} = \frac{2R_\mathrm{m}}{2R_\mathrm{m} + 2K_\mathrm{r}R_\mathrm{g}}\phi_\mathrm{r} \tag{4.1}$$

$$\phi_\mathrm{g} = \frac{K_\mathrm{l}}{1 + K_\mathrm{r}\frac{\mu_\mathrm{r} h_\mathrm{ag} A_\mathrm{m}}{l_\mathrm{s} A_\mathrm{g}}}\phi_\mathrm{r} \tag{4.2}$$

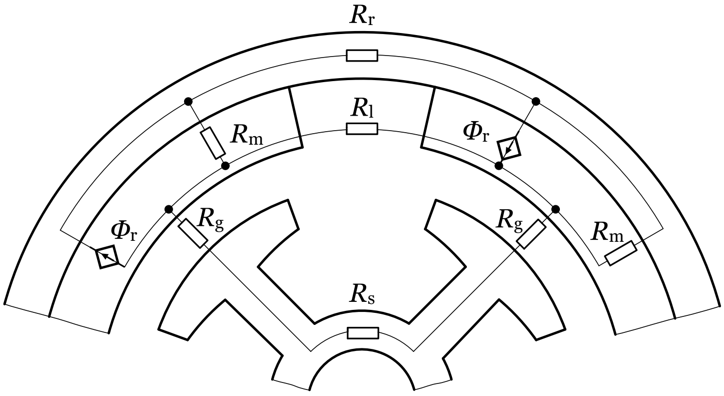

Figure 4.1: Model of stator and rotor with the used reluctances.

where the remanence flux is given by:

$$\phi_r = B_r A_m \tag{4.3}$$

The reluctances of the magnet (4.4) and the air gap (4.5) are calculated as follows:

$$R_m = \frac{h_{mg}}{\mu_0 \mu_r A_m} \tag{4.4}$$

$$R_g = \frac{h_{ag}}{\mu_0 A_g} \tag{4.5}$$

For well known standard machines K_l is normally in a range of 90 % to 100 % and K_r is in a range of about 1 to 1.2 [13, p. 73]. For small size motors and special machine geometries these factors generally do not hold anymore, and cannot be used for the design process. This leads to different calculation methods using MEC in the following sections.

4.3 Investigation of the Air Gap Reluctance

First, the air gap reluctance of the basic machine model has been investigated using the fringing effect from [13, p. 22-23]. This is the influence of the flux in the end zones of the air gap which increases the air gap area and so decreases the air gap

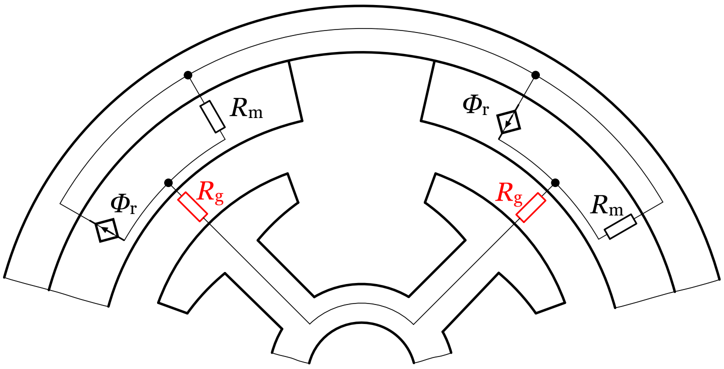

Figure 4.2: Basic machine model with air gap and inner magnet reluctance.

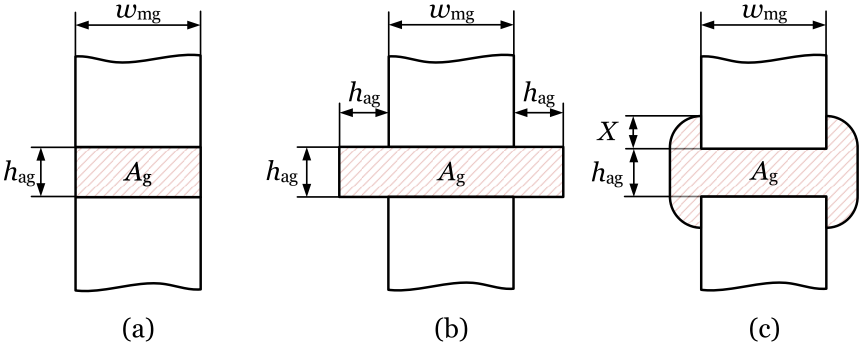

Figure 4.3: Fringing illustration considering (a) no fringing, (b) rectangular fringing, and (c) circular fringing from [13, p. 22-23].

reluctance.

Then, the air gap reluctance is calculated using (4.6)-(4.8). (4.6) calculates the air gap reluctance by using just the straight paths without any fringing flux components, see Fig. 4.3(a) from [13, p. 21]. In (4.7) the fringing effect is considered by increasing the air gap area by two times the air gap length, see Fig. 4.3(b) from [13, p. 22-23]. (4.8) calculates the air gap reluctance by adding two times a circular area to the straight area, see Fig. 4.3(c) from [13, p. 23-24]. Here X is the height of the fringing flux path of the magnet. Because of the small magnet height in this machine X is chosen as half of the air gap height. Here w_{mg}, h_{ag}, l_s, and h_{mg} are the motor dimensions as in Fig. 2.5 and μ_0 is the permeability of free space.

$$R_{\text{g,no fringing}} = \frac{h_{ag}}{\mu_0 w_{mg} l_s} \tag{4.6}$$

$$R_{\mathrm{g,rectangular\ area}} = \frac{h_{\mathrm{ag}}}{\mu_0 \left(w_{\mathrm{mg}} + 2h_{\mathrm{ag}}\right) l_{\mathrm{s}}} \tag{4.7}$$

$$R_{\mathrm{g,circular\ area}} = \left[\frac{\mu_0 w_{\mathrm{mg}} l_{\mathrm{s}}}{h_{\mathrm{ag}}} + \frac{4\mu_0 l_{\mathrm{s}}}{\pi} \ln\left(1 + \frac{\pi X}{h_{\mathrm{ag}}}\right)\right]^{-1} \tag{4.8}$$

Additionally, the air gap reluctance has been calculated from the adapted 2D-FEM model using Ampere's law:

$$R_{\mathrm{2D\text{-}FEM}} = \frac{H_{\mathrm{g}} h_{\mathrm{ag}}}{\phi_{\mathrm{g}}} \tag{4.9}$$

where H_{g} is the magnetic field strength in the air gap, h_{ag} is the mean air gap length and ϕ_{g} is the air gap flux. Tab. 4.2 shows the results for the analytically calculated air gap reluctances, as well as the 2D-FEM result for the air gap reluctance. Compared to the 2D-FEM calculated air gap reluctance, the reluctance calculated with (4.7) is the most accurate one and so is used for the further calculations. The remaining error can be explained by the asymmetric air gap of the FEM model, while the analytical calculations use a symmetric air gap.

Calculated Air Gap Reluctances			
No Fringing	$R_{\mathrm{g,no\ fringing}}$	7.07	MA/Vs
Fringing with Rectangular Area	$R_{\mathrm{g,rectangular\ area}}$	6.58	MA/Vs
Fringing with Circular Area	$R_{\mathrm{g,circular\ area}}$	6.91	MA/Vs
2D-FEM Result	$R_{\mathrm{2D\text{-}FEM}}$	5.79	MA/Vs

Table 4.2: Different calculated air gap reluctances compared to the 2D-FEM air gap reluctance.

4.4 Adding Rotor Leakage to the MEC

This Chapter extends the MEC, using the leakage flux terms of the magnets (especially the magnet to magnet and magnet to rotor flux leakage from [36]). Fig. 4.4 shows the model with the used reluctances for this extension. Here, R_m is the inner reluctance of the magnet, R_mr is the leakage reluctance from magnet to rotor, R_mm is the magnet to magnet reluctance, R_g is the air gap reluctance and ϕ_r is the flux source of the magnets. The magnetic circuit has been simplified by considering just one half of one pole pair (because of the symmetric MEC). This assumption and simplification from [36] leads to the magnetic circuit shown in Fig. 4.5, using four times (twice the half magnet) the inner magnet reluctance (4.10), two times the magnet to rotor reluctance (4.11), once the magnet to magnet reluctance (4.12) and again, four times (twice the half air gap) the air gap reluctance with fringing (4.7). The magnet flux (4.3) has been halved (half magnet) as well. The dimensions of the machine are used from Fig. 2.5 (or Tab. 2.1) and μ_rec is the relative permeability of the magnet.

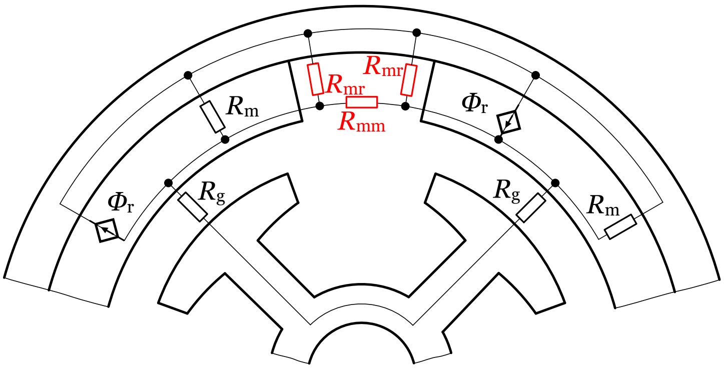

Figure 4.4: Model of the motor and the added reluctances of flux paths in red.

$$R_\mathrm{m} = \frac{h_\mathrm{mg}}{\mu_0 \mu_\mathrm{rec} w_\mathrm{mg} l_\mathrm{s}} \tag{4.10}$$

$$R_\mathrm{mr} = \frac{\pi}{\mu_0 \ln\left(1 + \frac{\pi h_\mathrm{ag}}{h_\mathrm{mg}}\right) l_\mathrm{s}} \tag{4.11}$$

$$R_\mathrm{mm} = \frac{\pi}{\mu_0 \ln\left(1 + \frac{\pi h_\mathrm{ag}}{w_\mathrm{mg}}\right) l_\mathrm{s}} \tag{4.12}$$

Solving this MEC using the current divider rule and the given reluctances leads to

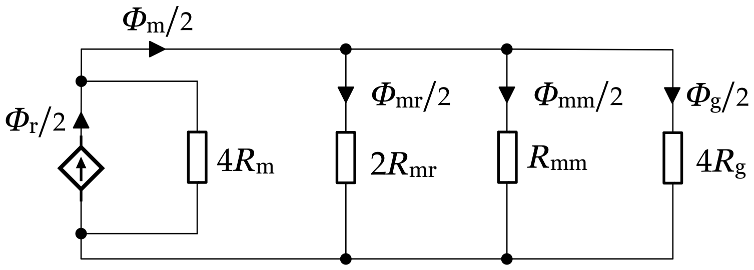

Figure 4.5: MEC of the motor model including rotor leakage.

the results of the flux paths and their percentage of the total flux, see Tab. 4.3. The magnet to magnet flux and the magnet to rotor flux has been united to the rotor leakage flux ϕ_{rl} to compare the results to the 2D-FEM simulation result. The leakage flux factor is the ratio of the air gap flux and the flux leaving the magnet (4.13), which is the percentage of the air gap flux in Tab. 4.3.

$$K_{lg} = \frac{\phi_g}{\phi_m} \tag{4.13}$$

The error (ϵ) of the analytically calculated fluxes compared to the adapted 2D-FEM simulation results is given in (4.14).

$$\epsilon = \left| 1 - \frac{\phi_{simulated}}{\phi_{analytical}} \right| \tag{4.14}$$

Even though the rotor leakage differs about 80 % to the FEM simulation the total error of the main flux paths differ just at about 20 %. This is caused by the relatively small percentage of the leakage flux compared to the total flux.

Flux Part	Symbol	Analytic Result	Percentage	Error to 2D-FEM
Magnet Flux	ϕ_m	14.74 μVs	100 %	19.7 %
Rotor Leakage Flux	ϕ_{rl}	0.49 μVs	3.3 %	81.5 %
Air Gap Flux	ϕ_g	14.25 μVs	97.7 %	18.8 %

Table 4.3: Analytically calculated fluxes including rotor leakage, their percentage of total and the error to 2D-FEM.

4.5 Adding Stator Leakage to the MEC

Next, the stator leakage, including stator tooth tip to stator tooth tip leakage and stator tooth to stator tooth leakage has been added to the model, see Fig. 4.6. The reluctance of the air gap and the magnet reluctances are calculated in the same way as shown in Chapter 4.4. But now the reluctance of the stator iron is not neglected anymore but computed using (4.15). Hence, the flux is passing through the stator iron the magnetic properties have to be considered with the relative permeability (μ_{stator}) of the used iron from the measured *BH*-curve from Appendix A.1.2 for a saturation of about 1.2 T (from the 2D-FEM model).

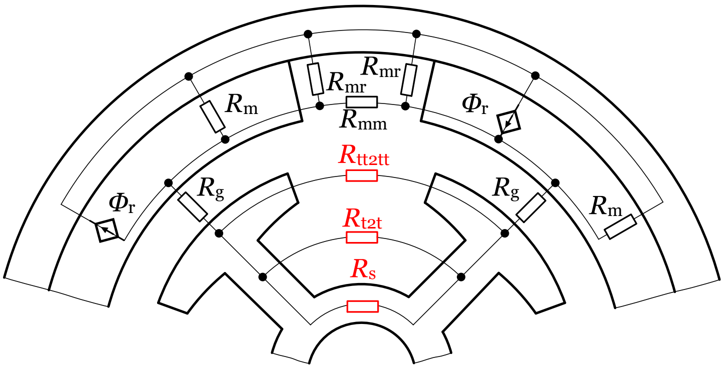

Figure 4.6: Expended model of the BLDC machine including and stator leakage in red.

$$R_{\mathrm{s}} = 4R_{\mathrm{stt}} + 4R_{\mathrm{st}} + R_{\mathrm{sy}} = 4\frac{d_1}{\mu_0\mu_{\mathrm{stator}}w_{\mathrm{tt}}l_{\mathrm{s}}} + 4\frac{d_3}{\mu_0\mu_{\mathrm{stator}}w_{\mathrm{tb}}l_{\mathrm{s}}} + \frac{w_{\mathrm{sy}}}{\mu_0\mu_{\mathrm{stator}}w_{\mathrm{sbi}}l_{\mathrm{s}}} \tag{4.15}$$

Here, R_{stt} is the reluctance of the stator tooth tip iron and is taken four times (twice because of two teeth in the circuit and twice because it is considered just the half pole). R_{st} is the reluctance of the stator tooth iron and is also taken four times. R_{sy} is the reluctance of the stator yoke. The tooth tip to tooth tip reluctance R_{tt2tt} and tooth to tooth reluctance R_{t2t} are given by [37]:

$$R_{\mathrm{tt2tt}} = \frac{w_{\mathrm{s}}}{\mu_0 d_1 l_{\mathrm{s}}} \tag{4.16}$$

$$R_{\mathrm{t2t}} = \frac{w_{\mathrm{cs}}}{\mu_0 d_3 l_{\mathrm{s}}} \tag{4.17}$$

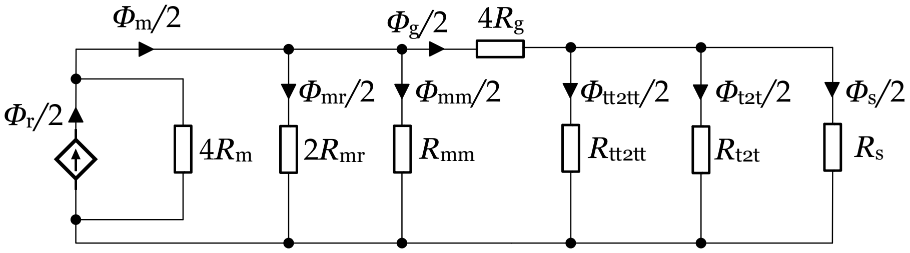

Figure 4.7: Extended MEC of the motor including stator leakage flux.

Fig. 4.7 shows the extended MEC for this case, including the stator reluctances. The current divisor rule has been used to calculate the fluxes for each path and the results, their percentage of the total flux and the error to the adapted 2D-FEM simulation results are shown in Tab. 4.4. This leakage flux factor is now the ratio of the stator iron flux ϕ_s to the magnet flux ϕ_m and is again shown as the percentage of the stator iron flux. The errors of the main flux paths are now in a range of 15 % compared to the 2D-FEM simulation results, although the leakage terms still differ at about 50 % and 70 % respectively, because of their relatively low percentage of the total flux they hence have low impact.

Flux Part	Symbol	Analytic Result	Percentage	Error to 2D-FEM
Magnet Flux	ϕ_m	14.23 μVs	100 %	16.8 %
Rotor Leakage Flux	ϕ_{rl}	0.51 μVs	3.6 %	47.1 %
Air Gap Flux	ϕ_g	13.72 μVs	96.4 %	15.7 %
Stator Leakage Flux	ϕ_{sl}	0.28 μVs	2.0 %	71.4 %
Stator Iron Flux	ϕ_s	13.44 μVs	94.4 %	14.5 %

Table 4.4: Calculated results for the fluxes, their percentage of total and the error compared to 2D-FEM.

4.6 Considering the Rotor Iron in the MEC

Next, the rotor back iron of the machine has been added to the magnetic circuit. This term typically can be neglected at large machine designs with no saturation effect because of the large permeability. As already mentioned in the previous Chapter, the manufacturing influence, as well as the saturation of the steel change its relative permeability. Also the distance of the magnetic paths in the rotor is larger, because of the inside out motor design, the rotor reluctance has been added for the analytic calculations, see Fig.4.8. The reluctance of the rotor back iron R_r is calculated by:

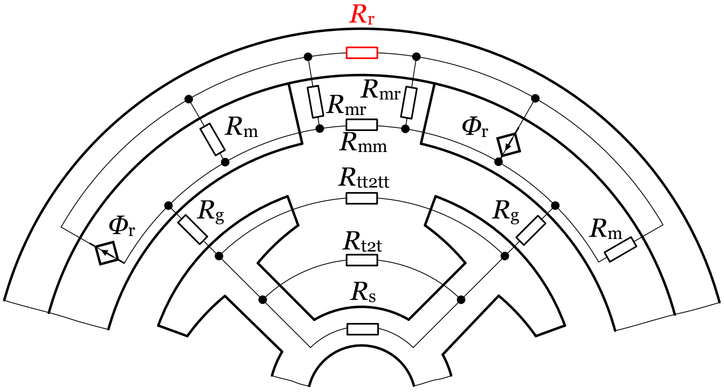

Figure 4.8: Model of the machine with rotor back iron reluctance consideration in red.

$$R_\mathrm{r} = \frac{w_\mathrm{ry}}{\mu_0 \mu_\mathrm{rotor} w_\mathrm{rbi} l_\mathrm{s}} \tag{4.18}$$

where w_ry, w_rbi and l_s are the motor dimensions given in Tab. 2.1 and μ_0 is the permeability of free space. μ_rotor is the permeability of the rotor steel and has been taken from the measured *BH*-curve (from Appendix A.1.1) for the given saturation at about 1.4 T (determined by 2D-FEM). The results obtained with MEC are shown in Tab. 4.5. The leakage terms of the analytic calculations have an error (compared to 2D-FEM) of about 50 % and 65 % respectively. The stator iron flux agrees very well, because the leakages are very small compared to the main flux parts. Most influence here is caused by the rotor and stator iron, because of their low relative permeability in this machine.

Flux Part	Symbol	Analytic Result	Percentage	Error to 2D-FEM
Magnet Flux	ϕ_m	12.15 μVs	100 %	2.6 %
Rotor Leakage Flux	ϕ_rl	0.52 μVs	4.3 %	48.1 %
Air Gap Flux	ϕ_g	11.63 μVs	95.7 %	0.5 %
Stator Leakage Flux	ϕ_sl	0.23 μVs	1.9 %	65.2 %
Stator Iron Flux	ϕ_s	11.40 μVs	93.8 %	0.8 %

Table 4.5: Calculated values for the magnetic fluxes, their percentage and the error to 2D-FEM including the rotor back iron.

4.7 Analytically Calculated Versus 2D-FEM Simulated Results

This section discusses the distribution of the analytically calculated values along the circumference from Chapter 4.6 and compares them to the 2D-FEM simulation results, including the magnet flux, the stator iron flux and the BEMF.

Magnet Flux

First, the magnet flux has been compared, see Fig. 4.9. While the analytically calculated magnet flux is (ideally) constant, the one of the 2D-FEM simulation varies with the circumference. This is caused by the total reluctance of the motor, which changes with the position of the rotor. These two fluxes are in a good range for this 2D case.

Stator Iron Flux

Fig. 4.10 shows the analytically calculated stator iron flux compared to the 2D-FEM simulation results. For the analytically calculated stator iron flux course the assumption from [13, p. 86] has been used, telling that the ideal flux course of the stator iron flux is trapezoidally shaped. The 2D-FEM simulated stator iron flux is illustrated and differs to the ideal flux curve due to the magnetization of the magnetic ring and the asymmetric air gap of the example case drive. Still, these two flux paths agree well.

BEMF

The computed BEMFs are shown in Fig. 4.11 and are the derivations of the stator flux linkage (ψ_s). They are calculated using Faraday's law of inductance (from Chapter 3 in [38]) given by:

$$u_\mathrm{EMF} = -2p\frac{d\psi_\mathrm{s}}{dt} = -2pN\frac{d\phi_\mathrm{s}}{dt} \tag{4.19}$$

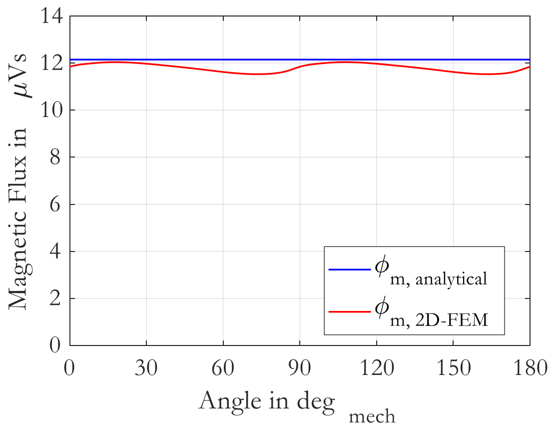

Figure 4.9: Magnet flux comparison, analytic versus 2D-FEM.

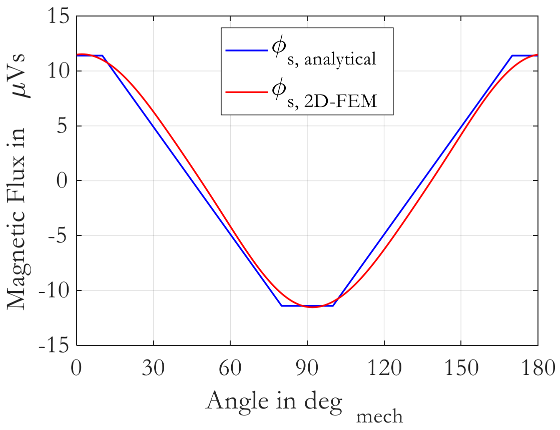

Figure 4.10: Stator iron flux comparison for the 2D case.

where ψ_s is the flux linkage of one phase, $2p$ is the number of poles, N is the number of turns per coil and ϕ_s is the stator iron flux. Since the linking stator iron flux for the analytical calculation is ideally trapezoid-shaped (seen Fig. 4.10), the BEMF (u_{EMF}) is rectangular shaped. To consider the asymmetric air gap for the analytically calculated BEMF, it has been computed for the smallest and largest distance of the asymmetric air gap. Then, the two forms have been combined and adapted to one curve. The 2D-FEM simulated BEMF is not ideally rectangular-shaped, which again are the effects of the asymmetric air gap and the magnetization of the magnetic ring. Nevertheless, the analytically and numerically determined values agree well.

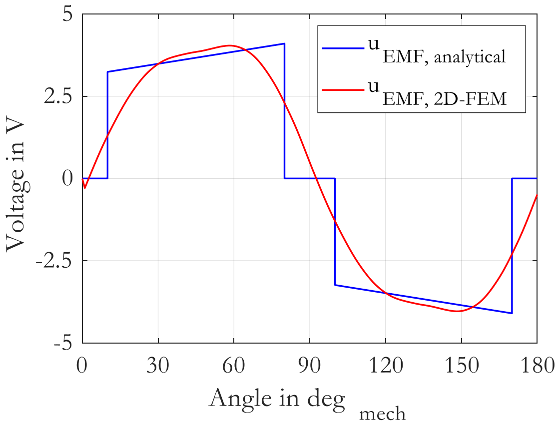

Figure 4.11: BEMF comparison (of one phase) for the 2D case.

4.8 Conclusion - 2D

Comparing the analytic calculations and extension steps from this Chapter show that the stator and rotor iron parameters, have the largest influence on the MEC, due to the relative poor magnetic properties of the steel caused by manufacturing process, as well as the high saturation of the material. So, it is important to consider these effects in the analytical calculation methods. Since these parameters are often not known in the design process, and also the flux density of the steel is not known, this makes it even more complicated to calculate the machine with analytic methods. On the other hand, Fig. 4.12(a) and Fig. 4.12(b) show the flux separation in percent of the analytical model and the 2D-FEM model respectively. Although the analytically computed leakage factor is almost twice the 2D-FEM computed leakage factor, the main flux terms including the magnet flux and especially the stator iron flux agree well. This is caused by the relatively low percentage of the leakage terms compared to the main flux parts. This means that, for a accurate prediction of the flux parts in the machine, these analytical methods are not useful but they do offer a quick estimation of the main flux terms.

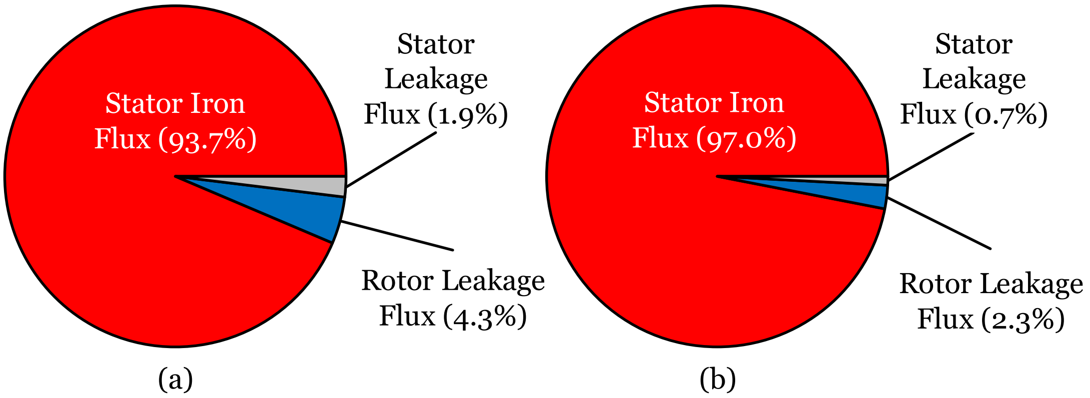

Figure 4.12: Flux separation of (a) the analytical model from Chapter 4.6 and (b) the 2D-FEM model.

Finally, the simulated 2D-FEM flux separation shows that the example case drive (neglecting rotor overhang and end face leakage) just has 3 % leakage. This was not expected and is small compared to the assumption of well known standard machine designs from [13], which indicates a range up to 10 % flux leakage.

Chapter 5

Three Dimensional Investigation of Stray Paths Using a MEC

This Chapters aim is to extend the MEC of the previous Chapter by the influence of the three dimensional leakage paths (including rotor overhang and stator end face leakage). First, the MEC from Chapter 4.6 has been considered and extended with rotor overhang effects. As a next step, the three dimensional stator leakage terms has been added to this MEC. For the extended MEC all flux paths has been calculated and compared to the 3D-FEM results form Chapter 3.5. For the analytical calculations the axial dimensions from Chapter 2.5 with different rotor and stator lengths have been considered.

5.1 Rotor Overhang Impact

First, the rotor overhang of the example case drive was considered. The MEC model from chapter 4.6 was extended by the overhang paths of the air gap, the inner magnet, the magnet to magnet and the magnet to rotor reluctances from [39]. Fig 2.5 shows the rotor overhang leading to extra flux paths in the air gap. The paths have been separated into a straight line flux and a circular flux path. To consider these flux paths an effective air gap length has been introduced from [39] given by:

$$h_{\mathrm{ag,eff}} = \begin{cases} \sqrt{h_{\mathrm{ag}}^2 + z^2} & \text{for} \quad 0 < z \leq h_{\mathrm{ag}} \\ \frac{1}{2}\pi z & \text{for} \quad h_{\mathrm{ag}} < z \leq l_{\mathrm{OH}} \end{cases} \tag{5.1}$$

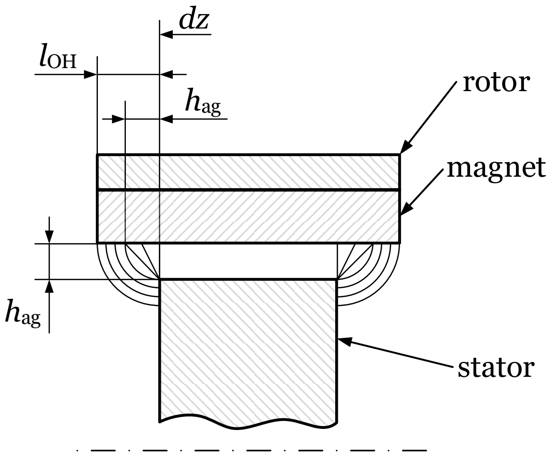

Figure 5.1: Rotor overhang and illustration of additional air gap flux paths from [39].

Then, (5.2) - (5.5) has been used to calculate the additional overhang reluctances.

$$R_{\mathrm{g,OH}} = \frac{h_{\mathrm{ag,eff}}}{\mu_0 \left(w_{\mathrm{mg}} + 2h_{\mathrm{ag,eff}} \right) dz} \tag{5.2}$$

$$R_{\mathrm{m,OH}} = \frac{h_{\mathrm{mg}}}{\mu_0 \mu_{\mathrm{rec}} w_{\mathrm{mg}} dz} \tag{5.3}$$

$$R_{\mathrm{mm,OH}} = \frac{\pi}{\mu_0 \ln \left(1 + \pi \frac{h_{\mathrm{ag,eff}}}{w_{\mathrm{ms}}} \right) dz} \tag{5.4}$$

$$R_{\mathrm{mr,OH}} = \frac{\pi}{\mu_0 \ln \left(1 + \pi \frac{h_{\mathrm{ag,eff}}}{h_{\mathrm{mg}}} \right) dz} \tag{5.5}$$

To solve these equations they have to be integrated with respect to dz (infinitesimal stack length), using the integration limits and the effective air gap length, where z starts from one side of the stator in the direction of the overhang. Due to the axial offset between rotor and stator iron of the example case drive, the overhang of both end sides is different. Therefore, the overhang reluctances have to be computed separately on both sides.

The rotor overhang causes additional reluctances (one straight line and one circular reluctance on each side), which are added parallel to the 2D-MEC reluctances (R_g, R_m, R_mr and R_mm) from Chapter 4.6. This leads to the three dimensional reluctances, for the overhang impact, the air gap, the inner magnet, the magnet to magnet and the magnet to rotor, respectively.

5.2 3D Stator Leakage Investigation

Next, the three dimensional flux paths of the stator end face are added to the 2D-MEC from Chapter 4.6 and the extended one from the previous Chapter, respectively. Again, the additional reluctances have been calculated and added to the main reluctances of the two dimensional case. The following approaches from [40, p. 127-132] have been used to calculate the additional 3D end face reluctances (for the stator tooth to stator tooth flux and the stator tooth tip to stator tooth tip flux). These flux lines are separated into a semicircular cylinder, see Fig. 5.2(a), a half annulus, see Fig. 5.2(b), a spherical quadrant, see Fig. 5.2(c) and a spherical shell part, see Fig. 5.2(d). For these parts (5.10) - (5.13) from [40, p. 127-132] have been used with their mean areas and the mean distances as follows:

$$A_\mathrm{sc} = \frac{\pi g^2 l}{8} \cdot \frac{1}{1.22g} = 0.322gl \quad \text{and} \quad l_\mathrm{sc} = 1.22g \tag{5.6}$$

$$A_\mathrm{ha} = xl \quad \text{and} \quad l_\mathrm{ha} = \pi\left(\frac{g+x}{2}\right) \tag{5.7}$$

$$A_\mathrm{sq} = \frac{\frac{1}{3}\pi\left(\frac{g}{2}\right)^3}{1.3g} = 0.1g^2 \quad \text{and} \quad l_\mathrm{sq} = 1.3g \tag{5.8}$$

$$A_\mathrm{ss} = \frac{\pi}{8}x\,(x+g) \quad \text{and} \quad l_\mathrm{ss} = \frac{\pi}{2}\,(x+g) \tag{5.9}$$

$$R_\mathrm{sc} = \frac{l_\mathrm{sc}}{\mu_0 A_\mathrm{sc}} = \frac{1.22g}{0.322\mu_0 gl} = \frac{3.789}{\mu_0 l} \tag{5.10}$$

$$R_\mathrm{ha} = \frac{l_\mathrm{ha}}{\mu_0 A_\mathrm{ha}} = \frac{\pi\,(g+x)}{2\mu_0 xl} = 1.57\frac{\left(\frac{g}{x}+1\right)}{\mu_0 l} \tag{5.11}$$

$$R_{\mathrm{sq}} = \frac{l_{\mathrm{sq}}}{\mu_0 A_{\mathrm{sq}}} = \frac{1.3g}{0.1\mu_0 g^2} = \frac{13}{\mu_0 g} \tag{5.12}$$

$$R_{\mathrm{ss}} = \frac{l_{\mathrm{ss}}}{\mu_0 A_{\mathrm{ss}}} = \frac{\frac{\pi}{2}(x+g)}{\mu_0 \frac{\pi}{8} x (x+g)} = \frac{4}{\mu_0 x} \tag{5.13}$$

Here g is the straight line distance from one to the other part of the flux and l is the length of the iron, see Fig. 5.2(e). Adding these additional reluctance parts to the main 2D reluctances (on both stator iron end faces) leads to the three dimensional reluctances for the stator leakage terms.

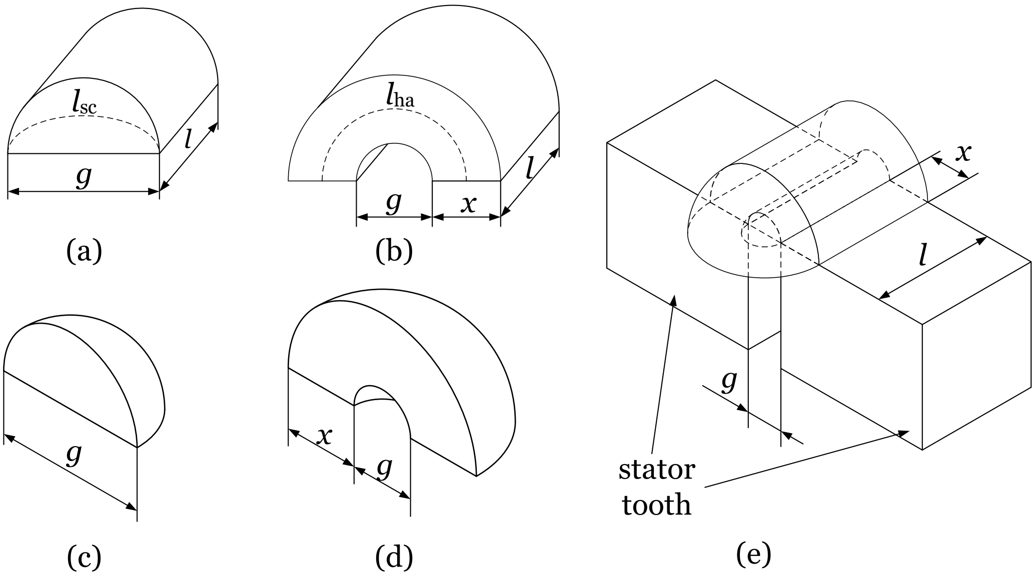

Figure 5.2: Leakage stray paths for (a) semicircular cyliner, (b) half annulus, (c) spherical quadrant, (d) quadrant of squerical shell and (e) the combination of these paths from [41].

5.3 Analytically Calculated Versus 3D-FEM Simulated Results

This section compares the analytically calculated results of the three dimensional extended MEC to the 3D-FEM simulated results from Chapter 3.5. For the analytical calculation, the relative permeability of the stator iron and rotor back iron were adjusted using the 3D-FEM flux density and the $\mu_r B$-curves form Appendix A.1. Tab.5.1 shows the results for the analytically computed values, their percentage of the total flux, as well as the error to the adapted 3D-FEM simulation results. While here the main flux terms differ more than 10 % compared to the 3D-FEM simulations, the leakage terms differ almost 120 % and 90 % respectively. The flux curves for the magnet flux, the stator iron flux, and the BEMF have been compared as well.

Flux Part	Symbol	Analytic Result	Percentage	Error to 3D-FEM
Magnet Flux	ϕ_m	17.29 μVs	100 %	10.2 %
Rotor Leakage Flux	ϕ_{rl}	0.72 μVs	4.2 %	118.1 %
Air Gap Flux	ϕ_g	16.57 μVs	95.8 %	15.6 %
Stator Leakage Flux	ϕ_{sl}	0.98 μVs	5.7 %	87.8 %
Stator Iron Flux	ϕ_s	15.58 μVs	90.1 %	11.0 %

Table 5.1: Analytically calculated results for the 3D investigation, their percentage of total and the error to 3D-FEM.

Magnet Flux

Fig. 5.3 shows the distribution of the magnet flux obtained by the analytical calculations and the 3D-FEM simulation. Again, the analytically calculated magnet flux is constant. The magnet flux of 3D-FEM varies in amplitude, as already mentioned in Chapter 4.7. The magnet fluxes differ about 10 %.

Stator Iron Flux

The distribution of the flux within the stator iron is modeled, using a DFT (Discrete Fourier Transformation) of the 3D-FEM simulated stator iron flux. Then, the DFT result was used to replicate the analytically calculated stator iron flux. Fig. 5.4 shows both stator iron fluxes.

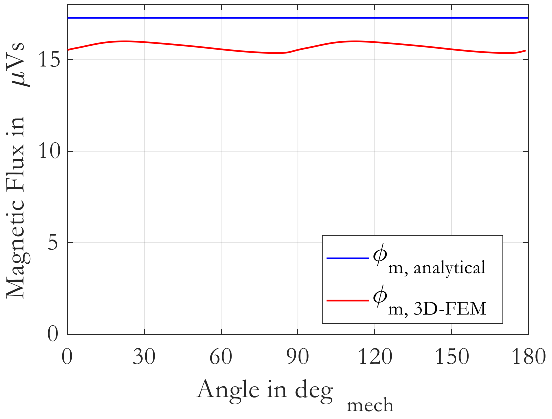

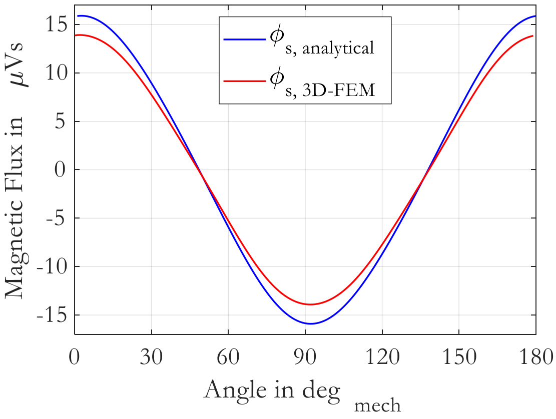

Figure 5.3: Simulated and analytically calculated magnet flux curves.

Figure 5.4: Simulated and analytically calculated stator iron flux curves.

BEMF

Fig. 5.5 shows the BEMFs per phase of the analytical case, respectively the 3D-FEM simulation result. The BEMF (u_{EMF}) for the analytical determination, again, has been calculated by deriving the stator fluxes with Faraday's law of induction from (4.19). Even by using a DFT to replicate the analytically computed stator iron flux for the waveforms, differ by about 10 %, which is a logical consequence of the difference in the computed fluxes.

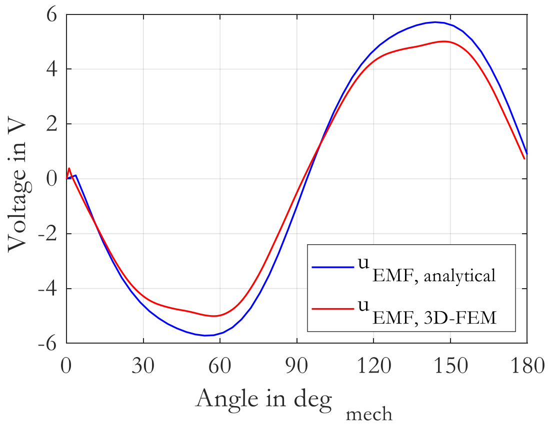

Figure 5.5: Simulated and analytically calculated BEMF of one phase.

5.4 Conclusion - 3D

Comparing the three dimensional analytically calculated results to the 3D-FEM simulation results, it is noticeable that the fluxes of the magnet and through the stator iron differ about 10 % compared to the 3D-FEM simulation results, even by considering the material parameters for the rotor and stator iron.

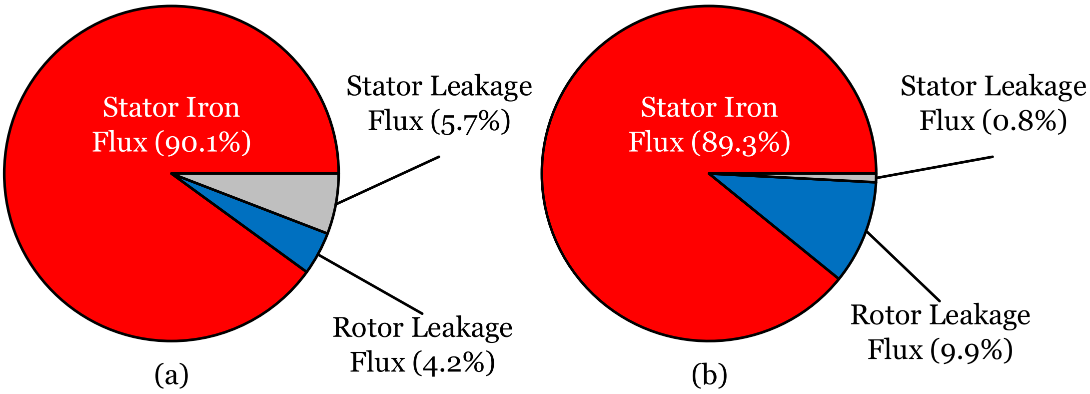

Figure 5.6: Flux separation of (a) the analytical model from Chapter 5.3 and (b) the 3D-FEM model.

Fig. 5.6(a) and Fig. 5.6(b) show the separation of the flux terms of the analytical model, respectively the 3D-FEM model. The leakage of both cases are in total in same range, but the rotor and stator leakage terms of both cases are totally different. While in the analytical model the rotor and stator leakage components are balanced, in the 3D-FEM model most of the leakage is determined by the rotor.
This leads to the result that the prediction of the flux distribution, especially the leakage flux terms, using simple analytical models is not accurate. While in the 2D case the main flux parts can be used for a quick estimation, the 3D case (including rotor overhang and end face leakage) does not offer accurate results.
Finally, considering the stray paths using the 3D-FEM model leads to about 10 % flux leakage of the example case drive. Compared to the leakage assumption from [13] for well known machine designs (in a range of 10 % - 20 %), shows only a small leakage pf the PM generated flux.

Chapter 6

Motor Inductance Investigation

This Chapter is concerned with the investigation of the inductance of the example case drive, especially its leakage parts. These leakage parts, in difference to the open circuit leakage parts, are affected by the flux produced by the coil current. The investigation starts with an overview of the inductance terms and the separation in a main part and in leakage parts. Moreover, a preliminary 3D-FEM investigation of the motor inductance neglecting the flux produced by the PM, has been realized. First, the data sheet parameters, but with the adapted magnetization from Chapter 3.3, have been used for the simultion. Then, again the parameters of the FEM model have been adapted, to identify the influence of each parameter on the machine inductance. Further on the flux produced by the PM has been considered, because it leads to saturation of the rotor and stator iron. After that the results of the 3D-FEM simulations have been compared to experimentally determined inductance of the example case drive. Because of the large difference between the 3D-FEM simulations and the measurements the parameters of the 3D-FEM model have been adapted step by step to identify the parameters of largest influence and to decrease the discrepancy. Finally, the inductance parts have been separated with the FEM model, using the adapted parameters. The leakage inductance of the example case machine is about 50 % of the total inductance.

6.1 Main Inductance Parts of a BLDC Motor

The inductance of a machine is an important parameter, e.g., for sensorless control of EC (electrically commutated) motors. It is directly proportional to the time constant and has an important influence on the current control. To obtain accurate results, mostly 3D-FEM analysis is used. Since many parameters do affect the inductance, e.g., the rotor position and so the saturation of the iron, its determination is not straightforward [27, p. 214].

In addition to the self inductance, also the mutual inductance has to be considered. In a multi phase machine it is about 10 % of the self inductance and is often neglected [13, p. 94]. In special cases (e.g., bifilar windings) the mutual inductance becomes as large as 100 % of the self inductance (investigated in Appendix A.2.3).

The investigated self inductance parts are [27, p. 214]:

- Air Gap Inductance (L_g)
- Slot Leakage Inductance (L_slot)
- End Turn Inductance (L_end).

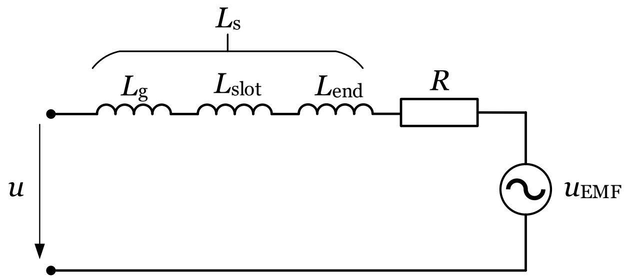

Figure 6.1: Equivalent circuit diagram of a BLDC machine with focus on leakage inductances.

Here, the air gap inductance corresponds to the flux which crosses the air gap, the slot leakage inductance does not pass the air gap but rather crosses over the slots of the stator and the end turn leakage encircles the end turns outside of the active air gap.

The flux produced by the coil current of the machine does not contribute to the flux produced by the permanent magnets. Hence the magnets are just blocks with relative permeability μ_r [13, p. 94-95].

The three inductance parts (air gap inductance L_g, slot leakage inductance L_slot and end turn inductance L_end), the coil resistance (R) and the BEMF (u_EMF) of the equivalent circuit diagram (for one phase) are shown in Fig. 6.1.

6.2 Preliminary Inductance Analysis

For the first investigations of the motor inductance a 2D and 3D finite element analysis has been realized. For these simulations, the FEM model from Chapter 3.3 was used. In preliminary investigations cross-coupling due to the magnet flux was neglected, meaning that the magnetic flux of the PM was not taken into account and the magnetic ring has been set to soft iron with its relative permeability. So the magnetic field in the machine is just caused by the coil current, to obtain a quick overview of the magnitude of the motor inductance.

Further on, the FEM simulations have been performed with constant coil current and different amplitudes. For the different amplitudes of the coil current the inductance of the machine has been analyzed using the known relationship of (6.1), where ψ is the flux linkage, $2p$ is the number of poles, N is the number of turns per coil and ϕ is the magnetic flux in the machine,

$$L = \frac{\psi}{I} = 2pN\frac{\phi}{I}. \tag{6.1}$$

Fig. 6.2 and Fig. 6.3 show the inductance depending on the coil current for one phase of the 2D-FEM model, respectively the 3D-FEM model. The inductance is constant for low coil current and decreases with increasing coil current, due to the saturation of the stator and the rotor iron. The difference between the 2D- and 3D-FEM simulation results is about 30 % and can be explained by the 3D effects (end turn winding and rotor overhang), which are not included in the 2D-FEM simulations.

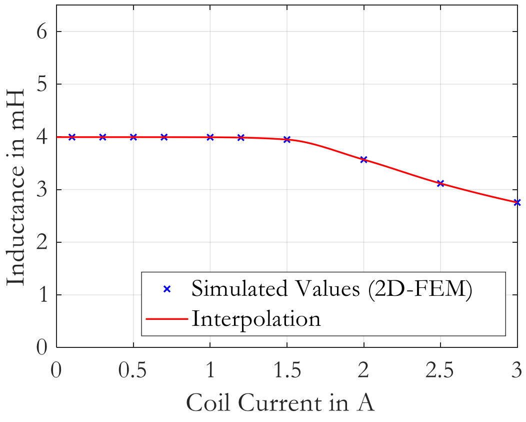

Figure 6.2: Inductance dependent on coil current in 2D-FEM.

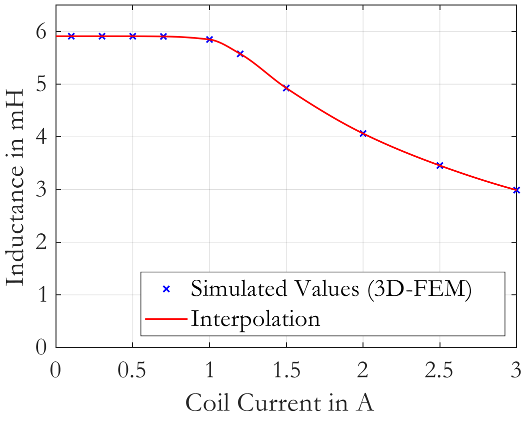

Figure 6.3: Inductance dependent on coil current in 3D-FEM.

6.3 Inductance Analysis at Certain Rotor Positions Including Magnet Cross-Saturation

The first case of inductance determination with finite element analysis was realized without considering the flux produced by the magnetic ring. In this case, the inductance of the machine has been investigated when the magnetic flux of the magnetic ring affects the stator and rotor iron in terms of their saturation and magnetic properties. The rotor is positioned and locked in three certain positions. The flux density distribution of the machine is shown in Fig. 6.4(a) for the rotor positions at 3 deg_{mech} and 48 deg_{mech}. The rotor position at 93 deg_{mech} leads to the same flux density distribution (but opposite flux direction) as at 3 deg_{mech}. Fig. 6.4(b) shows the 3D-FEM simulated stator iron flux waveform of the motor. The rotor position at 3 deg_{mech} (in direction of the asymmetric air gap) leads to the stator iron flux maximum. The position at 48 deg_{mech} is the rotor position, where the stator iron flux is zero, and the stator iron flux reaches its negative maximum at 93 deg_{mech}.

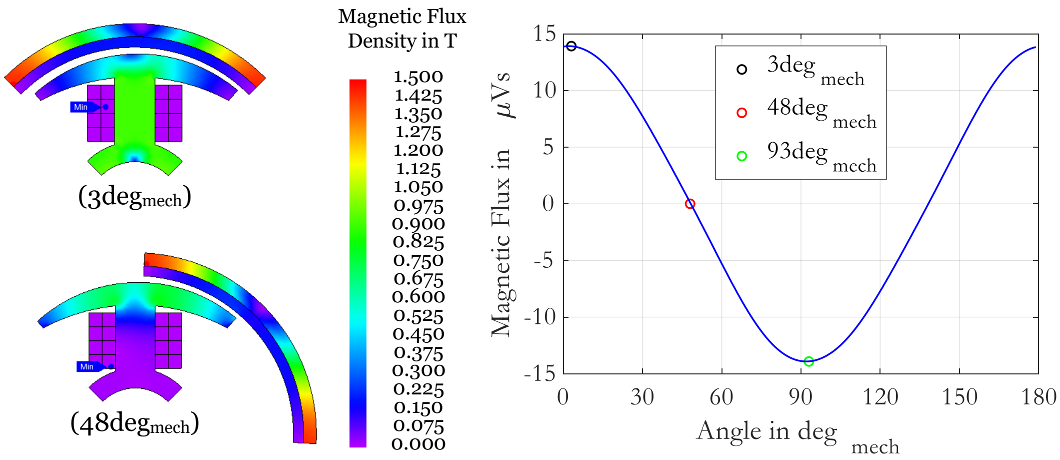

(a) (b)

Figure 6.4: 3D-FEM simulated (a) flux density distributions and (b) stator iron flux waveform at different rotor positions.

Another consideration for the inductance investigation is shown in Fig. 6.5, where (a) shows the current direction for positive and (b) the current direction for negative current. For the given direction of the stator iron flux (produced by the permanent magnet), a positive coil current leads to a flux in the same direction as the flux produced by the permanent magnets, see Fig. 6.5(a). This means that the total flux (from coil current and PM) leads to a higher saturation in the stator iron and the inductance of the machine is supposed to decrease. For a negative coil current the flux produced by the PM and coils are in opposite direction, see Fig. 6.5(b). This means that the total flux in the stator iron decreases which leads to less saturation and the inductance is supposed to increase. This can also be seen as the same effect with a negative maximum of the flux in the stator iron, produced by the PM. So by changing the flux in the stator to negative maximum, a positive coil current would decrease the flux density of the stator iron and for negative coil current would increase the flux desity in the stator. Because of the non linear characteristic of the machine, this leads to the difference for the rising and falling inductance in the following investigations. Since the inductances of booth phases of the machine are almost equal, just one phase has been considered in the next investigations.

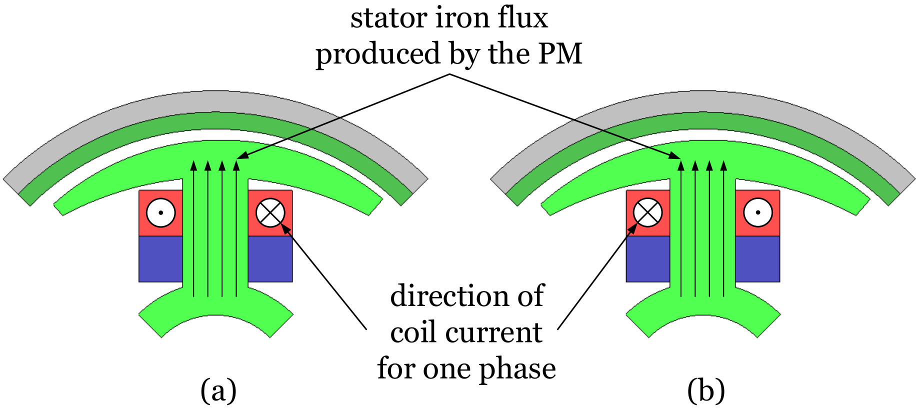

Figure 6.5: Coil current directions for (a) phase A and (b) phase B by a given stator iron flux.

6.4 Inductance Analysis with Rectangular Voltage

Two separate approaches of analysis were introduced. The first method is by supplying the coil of the machine with a rectangular voltage. The second method is by supplying the coil with a sine wave voltage to see the impact of lower (respectively no) harmonics in terms of eddy currents compared to the rectangular voltage. Since these two methods almost lead to the same results, the results of the sine wave approach are shown in Appendix A.2.

By providing a rectangular voltage to the coil a step response, where the inductance can be calculated from its time constant has been investigated. The exponential time curve of the current (seen Fig. 6.6), has been considered. After one τ (time constant) the current has reached 63 % for the rising edge (black markings in Fig. 6.7), respectively 37 % for the falling edge (green markings in Fig. 6.7). The inductance is calculated from the time constant of the step response as follows:

$$\tau = \frac{L}{R} \implies L = \tau R, \tag{6.2}$$

where R is the resistance of the coil and L is the inductance. The 3D-FEM simulations have been performed for the three different rotor positions. Since the results for both phases (phase A and B) are almost equal the investigations have just been analyzed for one phase. The amplitude of the voltage has been chosen with 1 V so that the coil current remains small in order to saturate the rotor and stator iron saturation too much and also operate close to the nominal current range of the example case drive. Tab. 6.1 shows the computed inductances of the machine for the three rotor positions. It is striking that the inductances at 3 deg_{mech} and 93 deg_{mech} respectively, are lower as the are at the position where the stator iron flux is zero (at 48 deg_{mech}). This is caused by saturation of the iron (caused by the flux of the magnetic ring) which reduces the permeability.

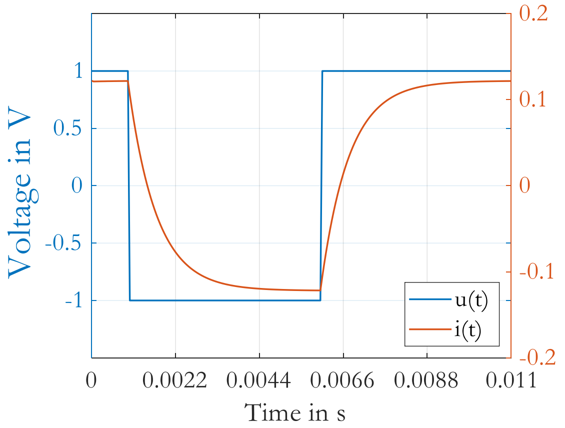

Figure 6.6: Simulated rectangular voltage and current course (3D-FEM) with absolute values.

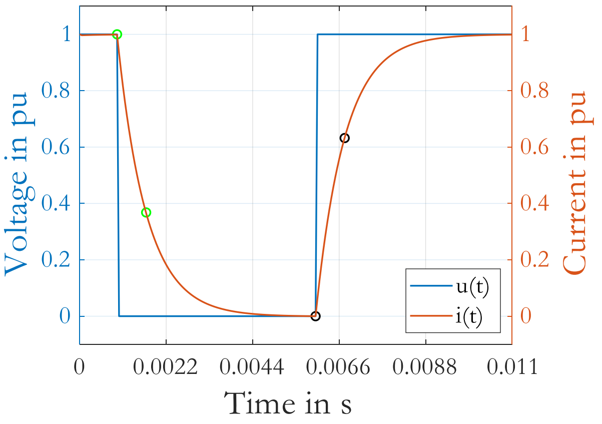

Figure 6.7: Adjusted courses (in p.u.) with illustrated time constant for rising and falling edge.

Voltage	Rotor Position	Simulated	
$\hat{U}$ in V	θ in deg_{mech}	L_{rise} in mH	L_{fall} in mH
1	3	5.5	5.2
	48	6.1	6.1
	93	5.2	5.5

Table 6.1: Inductance values for rectangular voltage at different rotor positions.

6.4.1 Measurement of the Motor Inductance

The 3D-FEM simulated results of the example case drive were compared to experimentally determined values. The experimental setup was the same as used for the BEMF measurement in Fig. 3.1. The only differences was a locked rotor in a certain position where a power amplifier provides the rectangular voltage to the coils. Further on, the coil voltage and the coil current of each phase have been measured. By measuring the time constant, the inductance has been calculated from (6.2). Tab. 6.2 shows the inductance L_{rise} for the rising edge and the inductance L_{fall} for the falling edge.

Voltage	Rotor Position	Measured		Error (3D-FEM)	
$\hat{U}$ in V	θ in deg_{el}	L_{rise} in mH	L_{fall} in mH	ϵ_{rise} in %	ϵ_{fall} in %
1	0	3.2	3.1	42	40
	90	4.4	4.4	27	27
	180	3.1	3.2	40	42

Table 6.2: Measured inductances for the rectangular voltage.

To compare the measured values to the simulate resutls , the errors (ϵ) have been calculated by:

$$\epsilon = \left| 1 - \frac{L_{\text{measured}}}{L_{\text{simulated}}} \right|$$

and are also shown in Tab. 6.2. The results of the measurements do not correspond well to the simulated ones from Tab. 6.1. This is mainly caused by the unadapted parameters of the FEM model, eventually leading to a FEM model adaptation.

6.5 FEM Model Adjustment and Further Investigations

The FEM model adjustment has been realized by changing the parameters (which have an impact on the inductance) in the FEM model subsequently, considering:

- Winding Configuration
- Eddy Current and Stator Lamination
- Stator Iron Material
- Rotor Iron Material

After every model adaptation the inductance has been computed by 3D-FEM and again compared to the measured results to identify the influence of every parameter.

6.5.1 Change of the Winding Configuration (II)

First, the winding configuration of the 3D-FEM model has been changed. Fig. 6.8(a) shows the coarse windings (approximated by two rectangular coils for the two phases), used in the previous simulations. Since this approximation seems to mismatch the reality a new coil model was implemented. Fig. 6.8(b) show the windings,

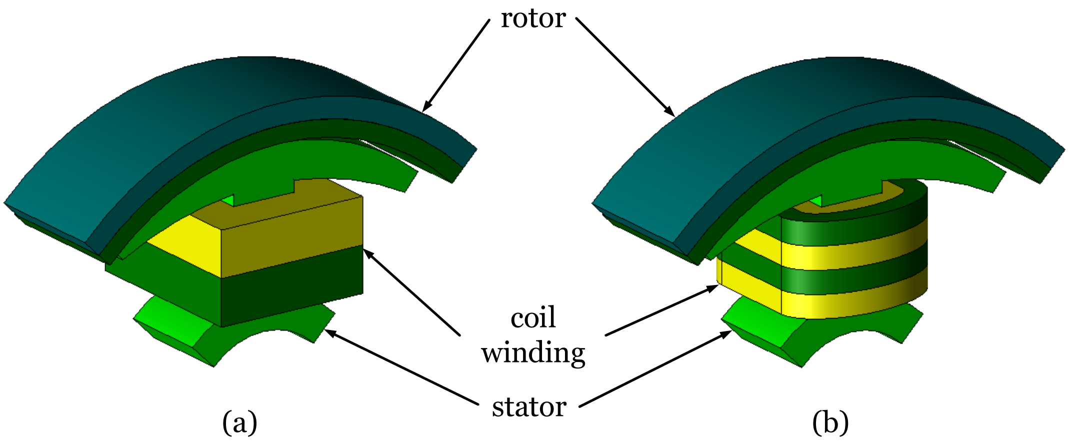

Figure 6.8: 3D-FEM model of (a) old winding configuration and (b) new winding configuration.

Voltage	Rotor Position	Simulated		Error	
$\hat{U}$ in V	θ in deg_{mech}	L_{rise} in mH	L_{fall} in mH	ϵ_{rise} in %	ϵ_{fall} in %
1	3	5.5	5.1	41	39
	48	6	5.9	26	26
	93	5.1	5.5	40	41

Table 6.3: Inductances for the adapted winding configuration.

split in smaller and crossed out coils, of course, with the same number of turns as before. Their rectangular form was changed in a rounder configuration, which should represent the bifilar winding more accurately. Tab. 6.3 shows the results for this case, again with the error to the measurements. Here, it could be observed that the modification of the coil setup did not have much effect on the inductance of the motor. This leads to further adaptations.

6.5.2 Simulation with Eddy Current and Stator Lamination (III)

Next, the influence of eddy currents in the stator iron was considered. To this aim, the properties of JMAG have been changed to consider the eddy currents for the worst case (no stator core lamination). Tab. 6.4 shows the results for this case and the errors to the measurements. The results show that eddy currents only slightly influence the inductance, for the example case machine.

Voltage	Rotor Position	Simulated		Error	
$\hat{U}$ in V	θ in deg_{mech}	L_{rise} in mH	L_{fall} in mH	ϵ_{rise} in %	ϵ_{fall} in %
1	3	5.1	4.9	38	37
	48	5.8	5.8	24	24
	93	5	5.1	38	37

Table 6.4: Inductances with eddy current consideration.

6.5.3 Impact of the Stator Iron Material (IV)

The the next, the stator iron properties were considered. As already mentioned in Chapter 3.4, an AC-test to determine the magnetic properties of the stator iron was performed. With these experimentally investigated magnetic parameters the simulations have been repeated and are shown in Tab. 6.5. By considering the correct parameters of the stator iron material, the error of the simulated inductance compared to the measured inductance decreases down to about 20 %.

Voltage	Rotor Position	Simulated		Error	
$\hat{U}$ in V	θ in deg_mech	L_rise in mH	L_fall in mH	ϵ_rise in %	ϵ_fall in %
1	3	4.2	3.9	24	20
	48	5.6	5.5	21	21
	93	3.9	4.2	20	23

Table 6.5: Inductance with adapted stator iron properties.

To evaluate the improvements of the 3D-FEM model for the inductance, another measurement was implemented. The rotor (including the magnetic ring and the rotor back iron) was removed and the inductance was measured again, see Tab. 6.6. The investigated stator iron material in Appendix A.1.2 was a laser cut ring with a glued stack, while the investigated motor does have a punched stator lamination connected with interlocking. Nevertheless the results without rotor of the 3D-FEM model (including the new winding configuration, the improved material of the stator iron and the impact of eddy current) fit well compared to the measurements. This motivated to also consider adaptation of the rotor parameters in a last step of analysis.

Voltage	Method	Rectangle	
$\hat{U}$ in V		L_rise in mH	L_fall in mH
1	Measurement	3.5	3.4
	Simulation	3.1	3.1

Table 6.6: Measured and simulated inductances of the stator without the rotor.

6.5.4 Impact of the Rotor Iron Material (V)

Due to the influence of the machining process also the rotor back iron has been investigated, using a DC-test (see Chapter 3.4 and Appendix A.1.1 respectively). Tab. 6.7 shows the 3D-FEM results, using the experimentally investigated magnetic parameters of the rotor back iron. Although the parameters of the 3D-FEM model have been adapted the difference to the measurement is still about 20 %. This can be caused by the non linear behavior of the machine, which makes it even more complex to determine the inductance.

Voltage	Rotor Position	Simulated		Error	
$\hat{U}$ in V	θ in deg_mech	L_rise in mH	L_fall in mH	ϵ_rise in %	ϵ_fall in %
1	3	4.1	3.8	22	18
	48	5.4	5.4	19	18
	93	3.8	4.1	18	22

Table 6.7: Inductance with adapted rotor back iron properties.

6.5.5 FEM Simulation Error Reduction

By adjusting the 3D-FEM models to better consider the machine's geometry and material parameters, the error of the 3D-FEM model has been cut in half. Fig. 6.9 and Fig. 6.10 show the relative error of the simulated inductance compared to the measured inductance for every modification step for the rotor postion at 3 deg_mech and 93 deg_mech respectively. The adaptation steps are marked in the Chapter title, where (I) is the 3D-FEM model with datasheet parameters (but the correct magnetization of the magnetic ring from Chapter 3.3), (II) is the new coil configuration, (III) is the eddy current impact, (IV) is the stator iron influence, (V) is the impact of the rotor back iron.

Other methods for the inductance investigation, e.g., using the stored energy from [42] could maybe lead to more accurate results.

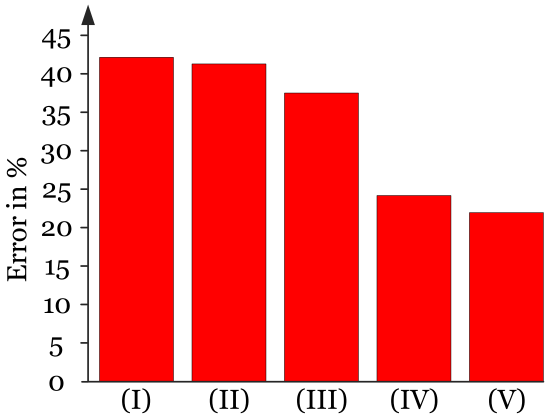

Figure 6.9: Inductance error reduction of 3D-FEM for rotor position θ at 3 $\mathrm{deg}_{\mathrm{mech}}$.

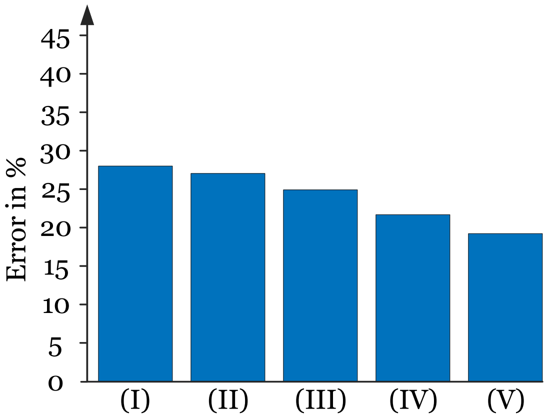

Figure 6.10: Inductance error reduction of 3D-FEM for rotor position θ at 48 $\mathrm{deg}_{\mathrm{mech}}$.

6.6 Separation of Inductance Parts

This section now aims to determine and separate the inductance parts with the use of the adapted FEM model (from Chapter 6.5.4). The main inductance parts for the separation are:

- Rotor Overhang Impact on the Inductance (L_{OH})
- End Turn Inductance (L_{end})
- Air Gap Inductance (L_{g})
- Slot Leakage Inductance (L_{slot})

In addition to the inductance terms mentioned before, the rotor overhang inductance is introduced here. This inductance considers the influence of the rotor overhang, which leads to less reluctance in the air gap and so the flux can pass the air gap more easily. These parts have been separated at the position of the rotor, where the stator iron flux is zero (at 48 $\mathrm{deg}_{\mathrm{mech}}$), because of two reasons. First, the inductance at this position is the most accurate, compared to the measured values. Second, the stator iron is not influenced by the magnetic flux of the permanent magnets. For the separation of the inductances a 2D- and 3D finite element analysis of the machine are needed. So, this position guarantees the same saturation of the stator iron for the

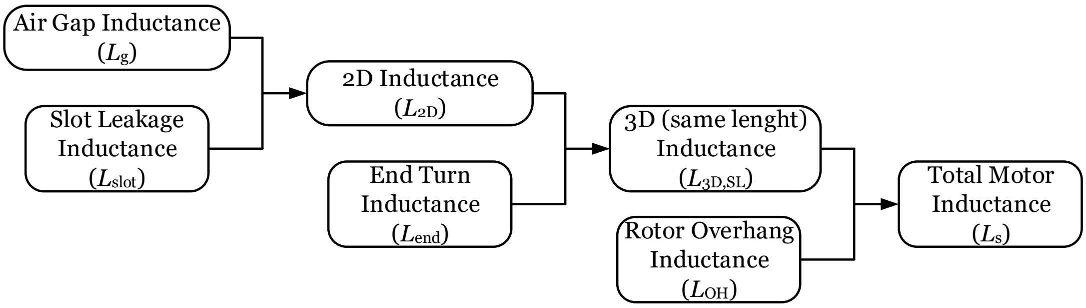

Figure 6.11: Flow chart of the inductance parts of the machine.

FEM models. Fig. 6.11 shows the relationship between the inductance terms, with L$_{2D}$, $L_{3D,SL}$ and $L_{3D,SL}$ discussed in the following sections.

6.6.1 Rotor Overhang Impact on the Inductance

First, the rotor overhang inductance is investigated, by creating another 3D-FEM model of the machine, where the axial length of the stator is equal to the length of the rotor (so a model without rotor overhang). This new model has the same magnetic parameters for the stator iron and rotor back iron, as well as the same winding configuration, see Fig. 6.12.

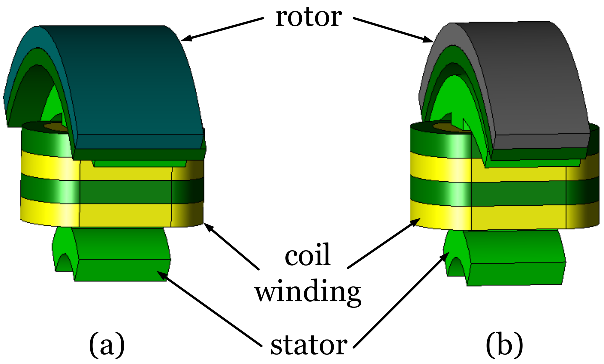

Figure 6.12: FEM motor model (a) with rotor overhang and (b) without rotor overhang.

Inspired by [43], the difference of the inductance from the 3D-FEM model (L_s) with rotor overhang to the 3D-FEM model with equal length for rotor and stator ($L_{\mathrm{3D,SL}}$) has to be the impact of the rotor overhang. Tab. 6.8 shows the result fo this inductance term.

6.6.2 End Turn Inductance

Next, the end turn inductance, using the consideration from [43] has been investigated. Here, the 3D-FEM model of the previous Chapter, where the stator and the rotor have the same axial length, has been considered and is again shown in Fig. 6.13(a). In addition to that, a 2D-FEM model has been created, with the same parameters used in the 3D-FEM model. A model as it is calculated in 2D-FEM is shown in Fig. 6.13(b), where the three dimensional end windings are not considered. As per [43], the difference of the inductances from the 3D model with same length ($L_{\mathrm{3D,OH}}$) and the 2D model (L_{2D}) approximately equals the inductance caused by the end windings. Again, the result for this case is shown in Tab. 6.8.

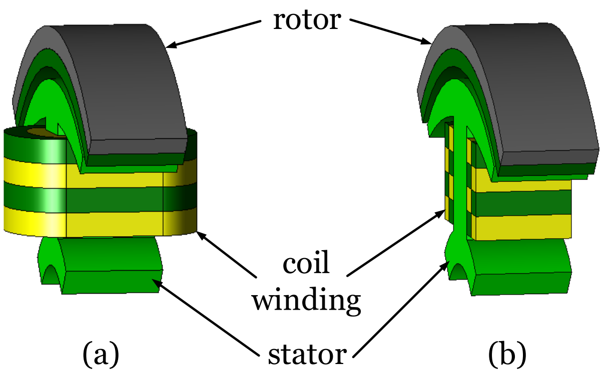

Figure 6.13: 3D-FEM model (a) of the machine with same length and (b) approximated model as calculated in 2D-FEM.

6.6.3 Air Gap Inductance

The air gap inductance is determined by using the 2D-FEM model. The air gap inductance is represented by the magnetic flux crossing the air gap and hence can be calculated by considering the magnetic flux crossing the air gap which is caused by the coil current as follows:

$$L_{\mathrm{g}} = 2pN\frac{\phi_{\mathrm{g}}}{I} \tag{6.3}$$

where L_{g} is the air gap inductance, $2p$ is the number of poles, N is the number of turns per coil, ϕ_{g} is the air gap flux and I is the coil current. The result is shown in Tab. 6.8.

6.6.4 Slot Leakage Inductance

After calculating the air gap inductance, the slot leakage inductance of the machine has to be the difference of the total inductance of the 2D-FEM model (L_{2D}) minus the air gap inductance L_{g}, because the other parts are not considered by the two dimensional finite element analysis. Tab. 6.8 again, shows the result.

6.6.5 Inductance Separation

After all inductance terms have been separated, the value and percentage (of total) of each term is shown in Tab. 6.8 and visualized in Fig. 6.14.

Inductance Part	Symbol	Value	Percent of Total
Air Gap Inductance	L_{g}	2.6 mH	49 %
Slot Leakage Inductance	L_{slot}	0.9 mH	16 %
End Turn Inductance	L_{end}	1.8 mH	33 %
Rotor Overhang Inductance	L_{OH}	0.1 mH	2 %
Total Motor Inductance	L_{s}	5.4 mH	100 %

Table 6.8: Illustration of the separated inductance parts and their percentage of total.

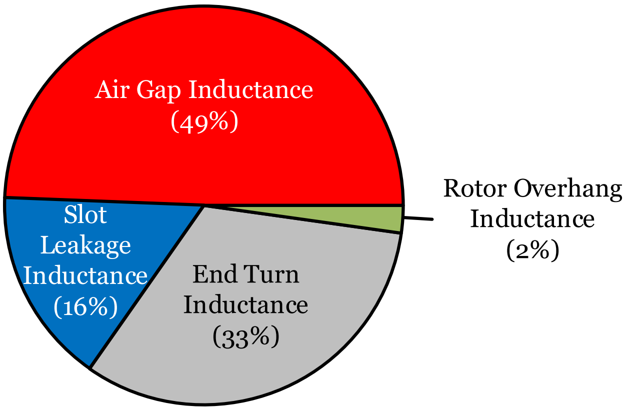

Figure 6.14: Separated inductances and their percentage of total.

The air gap inductance is in a range of about 50 % of the total inductance, while the slot leakage inductance is about 16 % and the end turn leakage is about one third. The rotor overhang is just 2 % of the total inductance, which leads to a total leakage inductance of about 50 %.

While the leakage paths of the example case drive due to the flux produced by the PM (from Chapter 3.5) is just about 10 %, the coil current affected leakage parts are about 50 %.

Chapter 7

Analytical Coil Inductance Investigation

This Chapter is concerned with the analytical calculation of the example case machine. The individual inductance parts have been calculated with the use of a MEC. To evaluate the analytical method the different calculated inductance parts have been compared to the inductances from Chapter 6.6. The results for the air gap and the slot leakage inductance are in an accurate range, while the rotor overhang inductance can get used as quick estimation and the end turn inductance has a large error and cannot be used for the calculation.

7.1 Air Gap Inductance

First, a MEC to calculate the air gap inductance from [13, p. 95-96] has been developed. Fig. 7.1 shows the model of one pole pair of the machine, where just the air gap reluctance and the inner magnet reluctance are considered. The magnets are considered as reluctances with a relative permeability ≈ 1. $N \cdot i$ is the magneto motive force (MMF) of each coil. Solving the MEC using the procedure from [13, p. 95-96] leads to the N^2P relationship as follows, where N is the number of turns, P is the permeance and $2p$ is the number of poles:

$$L_\mathrm{g} = \frac{2pN^2}{R_\mathrm{g} + R_\mathrm{m}} \tag{7.1}$$

The air gap reluctance is calculated with fringing effect from (4.7). Then, the air gap inductance is calculated. The result is shown in Tab. 7.1.

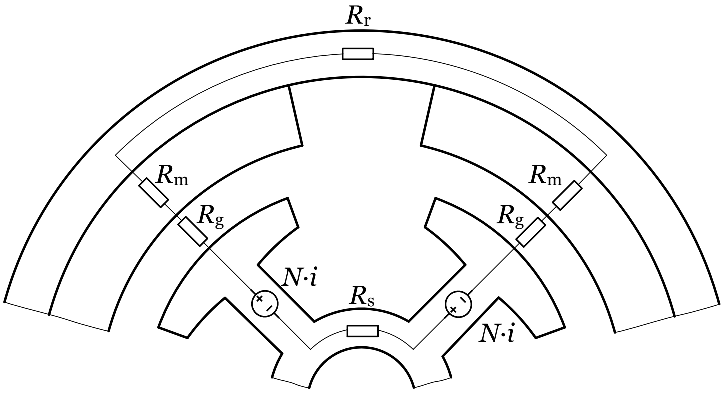

Figure 7.1: Model of the motor to calculate the air gap inductance.

7.2 Rotor Overhang Inductance

Additionally, the air gap inductance has been calculated for the rotor overhang with the air gap reluctance and the inner magnet reluctance from Chapter 5.1. The difference of these two air gap inductances (calculated with and without considering the rotor overhang) is the rotor overhang inductance, in Tab. 7.1.

7.3 Slot Leakage Inductance

Next, the slot leakage inductance from [13, p. 96-98] has been calculated. Again, the N^2P relationship has been used as follows:

$$L_{\mathrm{slot}} = 2p(2N)^2 l_{\mathrm{s}} \left[\frac{\mu_0 d_3}{3w_{\mathrm{cs}}} + \frac{\mu_0 d_1}{w_{\mathrm{s}}} \right] \tag{7.2}$$

This calculation leads to the result, shown in Tab. 7.1.

7.4 End Turn Inductance

The end turn inductance of the machine is calculated using a semicircular approximation of the end windings. Fig. 7.2(a) and Fig. 7.2(b) show the used model for this calculation, where τ_{cp} is the distance from the middle of one side of the coil to the middle of the other side of the coil and A_{s} is the cross-sectional area of the coil winding bundle. Therefore, the equation from [13, p. 100] was used:

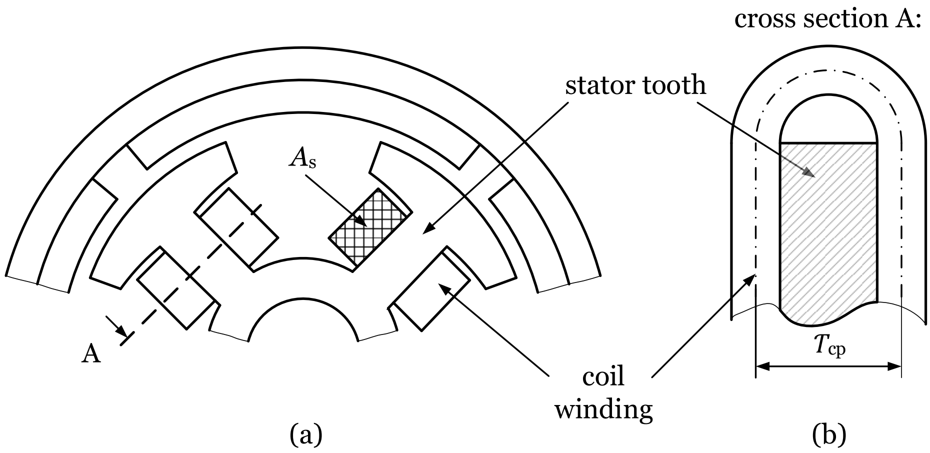

Figure 7.2: Model of (a) the BLDC with windings and (b) the cross section based on [13].

$$L_{end} = \frac{2p\mu_0\tau_{cp}N^2}{2}\ln\left(\frac{\tau_{cp}\sqrt{\pi}}{\sqrt{2A_s}}\right) \tag{7.3}$$

The result for the analytical calculation of the end turn inductance is shown in Tab. 7.1.

7.5 Comparison with FEM Simulated Results

Finally, all analytically calculated inductances are shown in Tab. 7.1, where the total motor inductance L_s is the sum of all individual inductances. To evaluate the analytic results, they were compared to the FEM simulated results from Chapter 6.6, using

Inductance Part	Symbol	Value	Error
Air Gap Inductance	L_g	2.2 mH	18 %
Slot Leakage Inductance	L_{slot}	1 mH	10 %
End Leakage Inductance	L_{end}	0.1 mH	1700 %
Rotor Overhang Inductance	L_{OH}	0.6 mH	83 %
Total Motor Inductance	L_s	3.9 mH	38 %

Table 7.1: Results for the analytical calculated inductance.

the error (ϵ) in (7.4).

$$\epsilon = \left| 1 - \frac{L_{\text{simulated}}}{L_{\text{analyrical}}} \right| \tag{7.4}$$

The error of the total machine inductance is about 40 % compared to the FEM simulated results. The analytic methods for the air gap inductance and the slot leakage inductance differ by about 18 %, and 10 % respectively compared to FEM and offer good results (keeping in mind that even the FEM model differs about 20 % to the measured value). On the other hand, the analytic results for the rotor overhang inductance differs more than 80 %, while the end turn inductance even differs about 1700 %. This means that the calculation methods for the air gap and the slot leakage inductance offer a good result while those for overhang and end turn inductances are not suitable to compute these inductances for the small drives of interest here.

Chapter 8

Conclusion and Future Work

8.1 Conclusion

Due to the increased need of fractional horsepower PM motors, especially in the automotive industry due to electrification or automated driving and the increasing demanding constraints like EMC and NVH, the design process of such machine types has become increasingly important. Because analytical calculations are often not accurate enough and finite element analysis takes too long, approximation based models may be introduced, however this kind of models need training to work well. This master thesis investigates the leakage paths of a fractional horse power PM motor. Therefore, an adaptation of a finite element model has been performed, by comparing the simulation results with measured values of a example case motor. The FEM model has been adapted step by step and the results of the simulations have been compared to the results of conventional analytical calculation methods.

The leakage paths determination has been separated in two different cases. The first case has been realized by an open circuit investigation of the machine to determine the leakage paths that affect the flux of the permanent magnet. Therefore, the FEM model has been improved in terms of the magnetic flux paths, magnetization of the magnets as well as the induced voltage. The results of the open circuit FEM simulations did match very well with the experimental investigations. Then, the analytical investigations, using the parameters of the adapted FEM model, has been considered. It was remarkable that for the two dimensional calculations with the use of magnetic equivalent circuits, the impact of the leakage paths do not have that much influence compared to the magnetic parameters of the used iron in the machine. For the three dimensional analytical calculation the same applies with larger difference compared to the FEM simulations.

The second case of the leakage determination was realized by the inductance investigations, to determine the leakage paths that affect the flux of the coil current. Here again, the FEM model was adapted to decrease the error compared to the measurements. And even though the error has been halved the simulation values differ about 20 % compared to the measured results. This could be mainly caused by the different manufacturing method (punching for the investigated motor versus laser cutting for the ring sample for measuring the magnetic properties) of the stator iron. Nevertheless, the inductance terms have been separated, eventually revealing that about 50 % of the total inductance can be attributed to leakage. Again, these results have been compared to the conventional analytical inductance calculations. Here the error between the simulation and the calculated results for the air gap and slot leakage inductance differ less, while the end turn and rotor overhang inductance do not come in a good accuracy and are not recommended as a solely basis for design. This master thesis solidly investigated stray paths in small PM motors but could not include all interesting questions. So a proposition for further investigations or research tasks, based on this work, could be:

- An investigation of the stator iron material, respectively the difference between the manufacturing steps punching and laser cutting, could be performed for the used material.
- An investigation of the deviation of the individual components, such as the stator, the rotor and the magnetic ring, in terms of their magnetic properties
- Other methods for the inductance determination could be investigated, for example with the use of the magnetic energy of the coils.
- The leakage investigations may be expanded to other motor dimensions and designs (sensitivity analysis).

Appendix A

Appendix

A.1 Investigation of Rotor and Stator Material

The magnetization properties of the used stator iron and rotor back iron (having different materials), were investigated. While the investigation of the rotor back iron is based on a DC-test (described in Appendix A.1.1), the stator iron investigation has been realized using an AC-test (described in Appendix A.1.2). Fig. A.1 shows the experimental setup for these measurements, including the data recorder for the measurements (I), the power amplifier to supply the setup (II), the power resistor to limit the current (III), the current sensor from [29] in (IV) and the investigated ring sample (V). Parts (II) and (III) are not shown in the picture in Fig. A.1(b).

A.1.1 DC-Test of the Rotor Iron

The back iron of the rotor has been investigated with a DC-magnetization test based on [44], because the flux in the rotor does not vary much and so the effects of eddy currents in the iron can be neglected. Instead of supplying the circuit with a fixed voltage and magnetizing the ring sample with different switch combinations, a magnetization curve, produced by the power amplifier (with a frequency of 1Hz) was supplied to the primary coil. On the secondary coil a flux meter (VI) (instead of a voltmeter for the secondary coil has been used in Fig.A.1(b)), which measures the magnetic flux by integrating the voltage, was connected. Here, the rotor back iron with a primary and secondary coil wound on it has been used as ring sample, based on the method from [45, p. 105-112].

Then, the magnetic field strength (A.1) and the magnetic flux density (A.2) have been calculated by the measured primary current and the measured magnetic flux,

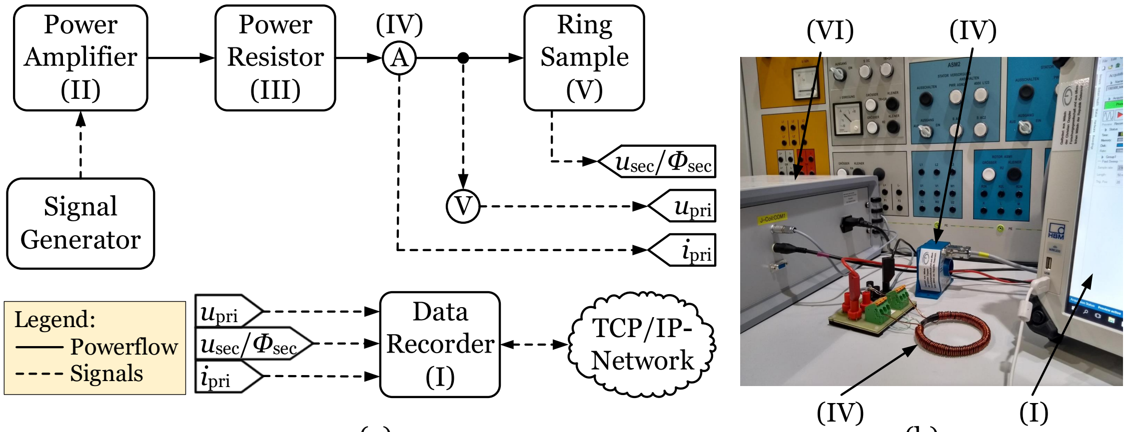

(a) (b)

Figure A.1: Experimental setup overview, (a) block diagram with voltmeter (u_{sec}) for the AC-test and fluxmeter (ϕ_{sec}) for the DC-test and (b) a picture of the test bench.

using the parameters and geometries of the rotor back iron from Tab. A.1 as follows:

$$H = \frac{N_{\mathrm{pri}} I_{\mathrm{pri}}}{l_{\mathrm{m}}} \tag{A.1}$$

$$B = \frac{\phi_{\mathrm{sec}}}{A_{\mathrm{r}}}, \tag{A.2}$$

Parameter		Value	Unit
Outer Diameter	D	27.5	mm
Inner Diameter	d	25.55	mm
Stack Length	w	5.75	mm
Primary Linding	N_{pri}	35	-
Secondary Winding	N_{sec}	50	-
Material	-	11SMnPb30	-

Table A.1: Parameters and dimensions of the rotor back iron for the DC-test.

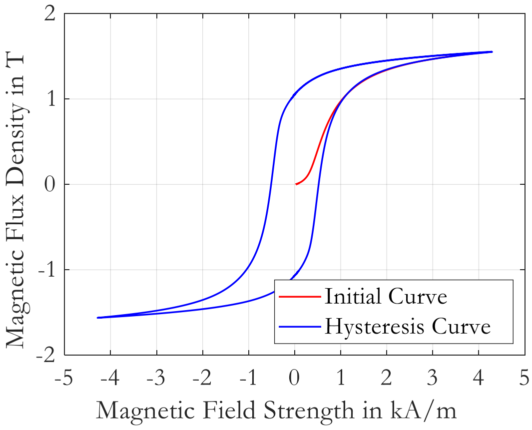

Figure A.2: Hysteresis curve of the rotor back iron with the DC-test.

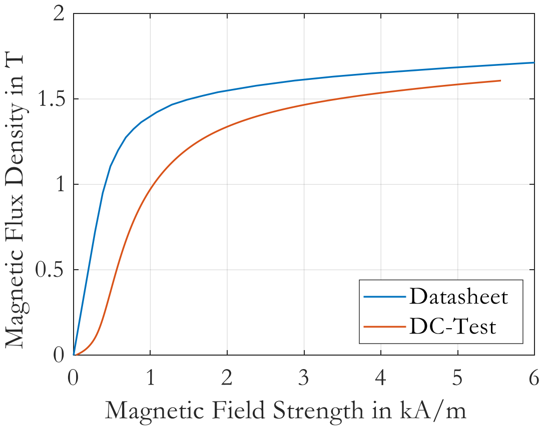

Figure A.3: Compared *BH*-curves of the rotor back iron.

where I_{pri} is the current of the primary coil, l_{m} is the average circumference of the rotor back iron, ϕ_{sec} is the flux measured on the secondary coil and A_{r} is the cross section of the rotor back iron. Fig. A.3 shows the initial magnetization curve as well as the hysteresis loop. The material used for the rotor back iron is soft magnetic. Fig. 3.9 shows the experimentally investigated $\mu_{\mathrm{r}}B$-curve, derivated from the initial magnetization curve, and the $\mu_{\mathrm{r}}B$-curve for the datasheet values. Due to datasheet uncertainty or manufacturing stress the relative permeability of the material decreases, compared to the datasheet values.

A.1.2 AC-Test of the Stator Iron

The stator iron has been investigated, using an AC-magnetization test based on [46]. The flux in the stator does vary with time and so eddy currents can have effects on the steel, as described in [47, p. 257-271]. In difference to the rotor investigations not the real stator, but a ring sample, with the same material and the given geometries and parameters (see Tab. A.2), has been investigated. The experimental setup for this investigation is almost the same as used in the DC-test. The differences were that the primary coil was supplied by a sine wave voltage and instead of measuring the flux of the secondary coil, the voltage (u_{sec}) has been measured. Then, the magnetic field strength has been calculated with (A.1). The analysis of the flux density of the ring sample has been submitted to post processing with (A.3) from [48].

$$B = \frac{1}{N_{\mathrm{sec}} A_{\mathrm{r}}} \int u_{\mathrm{sec}} dt \tag{A.3}$$

Then the *BH*-curves for different frequencies have been investigated. Fig. A.4 and Fig. A.5 show the *BH*-curves (hysteresis loop) for 50 Hz, and 200 Hz respectively, where the hysteresis loop for 50 Hz is smaller than the loop at 200 Hz, due to the impact of eddy currents in the material. Since the initial magnetization curve was not included in the measurement, it has been determined by averaging the hysteresis

Parameter	Symbol	Value	Unit
Outer Diameter	D	88.2	mm
Inner Diameter	d	77.6	mm
Stack Length	w	4.12	mm
Primary Winding	N_{pri}	111	-
Secondary Winding	N_{sec}	209	-
Material	-	M250-35A	-

Table A.2: Parameters and dimensions of the ring sample for the AC-test.

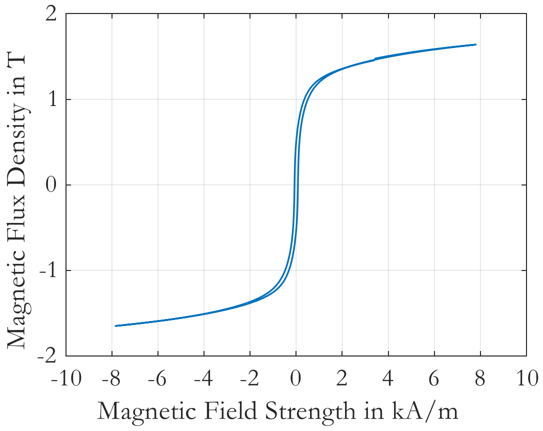

Figure A.4: Hysteresis curve of the stator ring sample at 50 Hz.

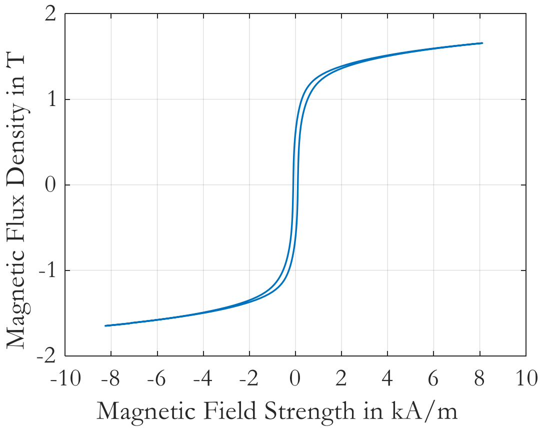

Figure A.5: Hysteresis curve of the stator ring sample at 200 Hz.

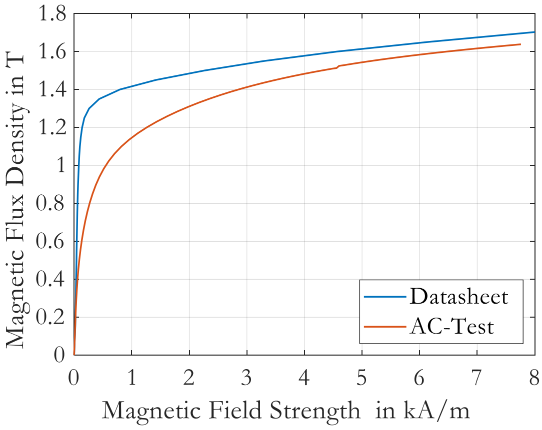

Figure A.6: Compared *BH*-curves of the stator ring sample for 50 Hz.

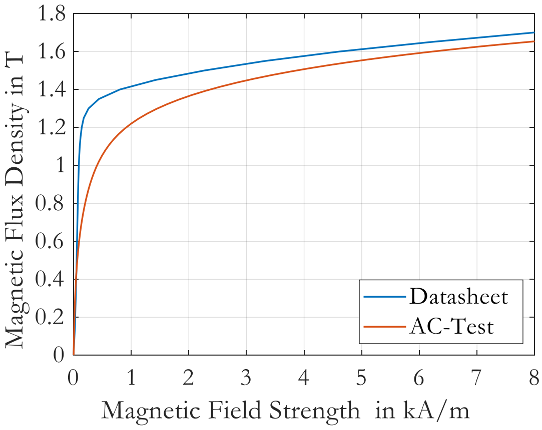

Figure A.7: Compared *BH*-curves of the stator ring sample for 200 Hz.

curve (for a first-order approximation). Fig. A.6 and Fig. A.7 show the *BH*-curves for the datasheet values and the experimental investigated results for 50 Hz, and 200 Hz respectively. Again, the difference between the processed and unprocessed material is quite large. Fig. A.8 and Fig. A.9 show the relative permeability depending on the magnetic flux density at 50 Hz and 200 Hz of the datasheet values compared to the measurements.

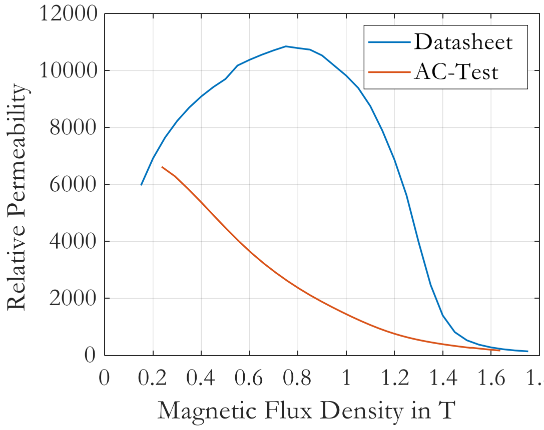

Figure A.8: Compared $\mu_r B$-curves of the stator ring sample for 50 Hz.

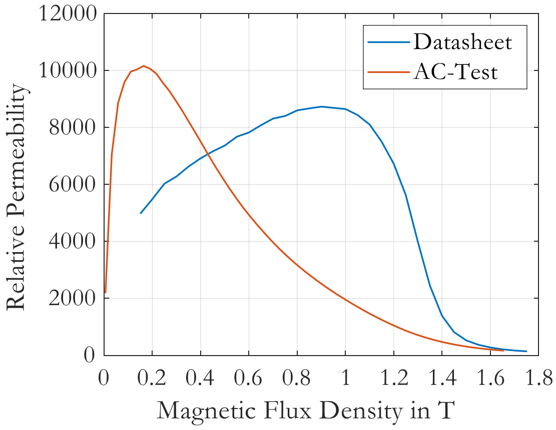

Figure A.9: Compared $\mu_r B$-curves of the stator ring sample for 200 Hz.

Since electric motors often operate in a range of 1 T to 1.5 T, the influence of the manufacturing process on the steel material parameters can be enormous.

A.2 Inductance Investigation with Sine Voltage

In analogy to Chapter 6, the inductance of the machine has been investigated, by supplying the coil with a sine wave voltage. Then, the current has been considered and the inductance has been calculated from the impedance. The inductance has been investigated experimentally and the results are compared to the adapted 3D-FEM model. Again, the error of both methods has been compared. Next, the inductance parts have been separated with the adapted FEM model. Eventually, the mutual inductance of the machine has been determined with experimental investigations and 3D-FEM simulations.

A.2.1 Measured Inductance Versus Adapted Simulation Results

The coils of the machine have been supplied with a sine wave voltage, which causes a sine shaped current, see Fig. A.10. Then, the inductance was calculated with (A.4). Therefore the impedance was calculated form the root mean square of the voltage and current. The same rotor positions, as well as the same amplitude of the voltage as described in Chapter 6 have been investigated.

$$|Z| = \sqrt{R^2 + (\omega L)^2} \implies L = \sqrt{\frac{|Z|^2 - R^2}{\omega^2}} \quad \text{with} \quad Z = \frac{U_{\text{eff}}}{I_{\text{eff}}} \tag{A.4}$$

Another method to evaluate the inductance is by using a Fourier analysis of the

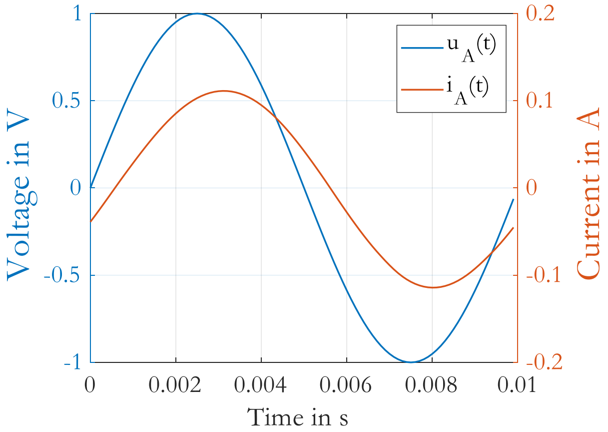

Figure A.10: Voltage and current of one phase coil.

coil voltage and the coil current, using a DFT. Then, the fundamental wave of the voltage and current have been determined, and again the impedance and the inductance have been calculated from (A.4). Because the simulated voltage and current waveforms do not have many harmonics the results are almost the same as the results calculated by the RMS values of the signals.

Voltage	Rotor Position	3D-FEM Simulated		Measured	
$\hat{U}$ in V	θ in deg_{mech}	L_{RMS} in mH	L_{DFT} in mH	L_{RMS} in mH	L_{DFT} in mH
1	3	4.6	4.7	3.4	3.4
	48	6	6	4.8	4.8
	93	4.6	4.7	3.3	3.3

Table A.3: Inductance of the adapted 3D-FEM model versus experimental investigations.

Tab. A.3 shows the results for the 3D-FEM simulations with the adapted parameters compared to the measured results for the RMS and DFT method. The inductances of the sine wave method are larger than thosedetermined from the supply with rectangular voltage. This is assumed to be the effect of increased eddy currents in the stator and rotor steel, because of more harmonics of the rectangular voltage compared to the sine wave voltage. The error of the simulated values compared to the experimentally investigated results are, again, in a range of about 20 %.

A.2.2 Stray Paths Separation

Inductance Part	Symbol	Value	Percent of Total
Air Gap Inductance	L_g	2.7 mH	45 %
Slot Leakage Inductance	L_{slot}	1.1 mH	18 %
End Turn Inductance	L_{end}	2 mH	33 %
Rotor Overhang Inductance	L_{OH}	0.2 mH	4 %
Total Motor Inductance	L_s	6 mH	100 %

Table A.4: Separated inductance parts of the machine for the sine voltage method.

With the adapted FEM model the inductance of the machine has been separated (see Chapter 6.6) for the rotor position at 48 deg_{mech}. Tab. A.4 and Fig. A.11 show the inductance parts separated in air gap, slot leakage, rotor overhang and end turn inductance. Again, the leakage part of the inductance is about 50 %.

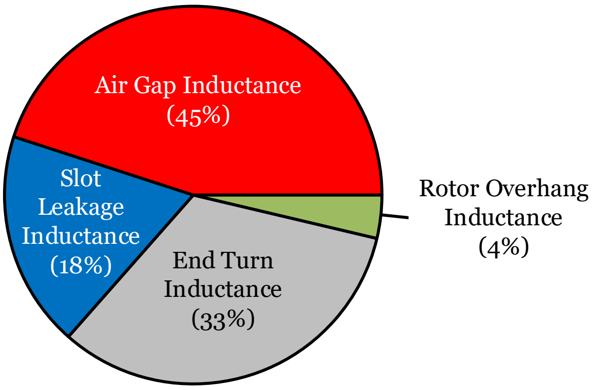

Figure A.11: Illustrated inductance parts from Tab A.4.

A.2.3 Mutual Inductance Investigation

In addition to the self inductance of the machine also the mutual inductance has been investigated. It is an important term in bifilar wound machines, because it determines the energy, which is transferred between the two phases while switching. To this aim, the sine wave approach has been used. While for the self inductance the voltage and current of one phase is considered (u_{A} and i_{A}), the mutual inductance is the influence from one coil to the other coil (u_{B} and i_{A}). The investigation has been realized, again, at a rotor position at 48 deg_{mech} (see Chapter 6.6). Fig. A.12 and Fig. A.13 show the sine wave current of one phase of the machine, which causes the voltage in the other phase of the machine for the measured case, and the 3D-FEM simulated case respectively. Then, the mutual inductance is calculated, using (A.5) from [49].

$$M = \left| \frac{U_B}{jwI_A} \right| \tag{A.5}$$

Here, I_{A} is the current of one phase, U_{B} is the induced voltage of the other phase and w is the angular frequency of the signals. Tab. A.5 shows the results for the

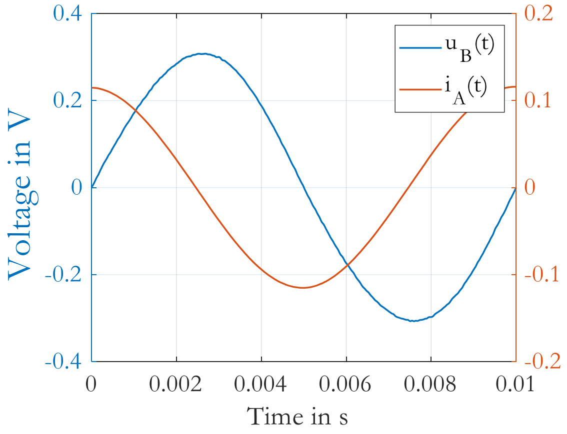

Figure A.12: Measured voltage and current for mutual inductance calculation at 48 $\deg_{\text{mech}}$.

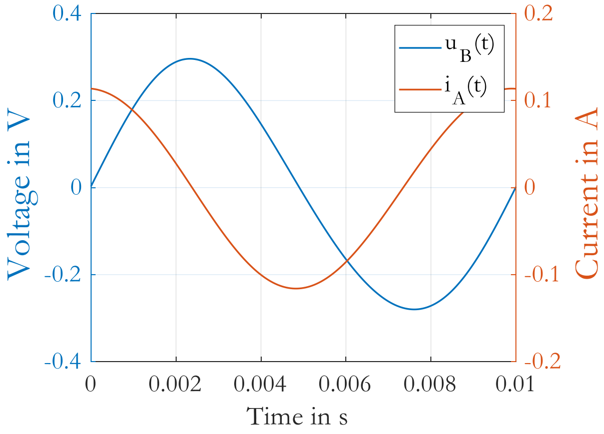

Figure A.13: Simulated voltage and current for mutual inductance calculation at 48 $\deg_{\text{mech}}$.

Parameter	Symbol	3D-FEM Simulated	Measured
Self Inductance	L	6 mH	4.8 mH
Mutual Inductance	M	5.3 mH	4.2 mH
Mutual to Self Ratio	M/L	88 %	88 %

Table A.5: Inductance of adapted 3D-FEM model versus experimental investigations.

self inductance, the mutual inductance and the mutual to self inductance ratio of the simulated, and the measured results respectively. The error of the mutual inductance is about 20 % between the experimental investigation and the FEM simulated results. The ratio of the mutual inductance to the self inductance is for both cases 88 %. Since the example case drive is bifilar wound the mutual inductance is ideally assumed to be 100 % percent of the self inductance. This means that the stray inductance of the mutual inductance of this machine is about 12 %.

Bibliography

[1] A. Kunz, M. Kunz, H. Vollert, and M. Förster, "Electromechanical Brake Booster for all Drive Concepts and Automated Driving," *ATZ worldwide*, vol. 120, no. 4, pp. 58–61, Apr. 2018.

[2] S. Chowdhury, L. Leitzel, and M. Zima, "Thermal System for Electric Vehicles with Coolant-based Heat Pump," *ATZ worldwide*, vol. 121, no. 5, pp. 48–53, May 2019.

[3] J. Hirt, "Cooling and Dehumidification of LED Headlights," *ATZ worldwide*, vol. 116, no. 5, pp. 36–39, May 2014.

[4] A. Reul, K. Fecke, and H. Stobrawe, "Adjustable Oil Pump for the Lubrication of Transmissions," *ATZ worldwide*, vol. 116, no. 12, pp. 30–35, Nov. 2014.

[5] G. Bramerdorfer, J. A. Tapia, J. J. Pyrhönen, and A. Cavagnino, "Modern Electrical Machine Design Optimization: Techniques, Trend, and Best Practices," *IEEE Transactions on Industrial Electronics*, vol. 65, no. 10, pp. 7672–7684, Feb. 2019.

[6] S. Silber, W. Koppelstätter, G. Weidenholzer, G. Segon, and G. Bramerdorfer, "Reducing Development Time of Electric Machines with SyMSpace," in *2018 8th International Electric Drives Production Conference (EDPC)*, Dec. 2018, pp. 1–5.

[7] H. Grübler, S. Leitner, A. Muetze, and G. Schoener, "Improved Switching Strategy for a Single-Phase Brushless Direct Current Fan Drive and its Impact on Efficiency," *IEEE Transactions on Industry Applications*, vol. 54, no. 6, pp. 6050–6059, Nov. 2018.

[8] H. O. Seinsch, *Grundlagen elektrischer Maschinen und Antriebe*, 3rd ed. Springer Fachmedia Wiesbaden, 1993.

[9] H. Hembach, "Systematischer Vergleich von BLDC-Motorkonzepten mit Anwendung auf nass laufende Wasserpumpen kleiner Leistung," Ph.D. dissertation, Universität der Bundeswehr München, 2007.

[10] S. Hofmann, "Noise, Vibration, and Harshness - Characteristics of Sub-Fractional Horsepower Fan Drives," Master's thesis, Electric Drives and Machines Institute - Graz University of Technology, 2019.

[11] T. Lee, M. Seo, Y. Kim, and S. Jung, "Motor Design and Characteristics Comparison of Outer-Rotor-Type BLDC Motor and BLAC Motor Based on Numerical Analysis," *IEEE Transactions on Applied Superconductivity*, vol. 26, no. 4, pp. 1–6, June 2016.

[12] S. Sakunthala, R. Kiranmayi, and P. N. Mandadi, "A study on industrial motor drives: Comparison and applications of PMSM and BLDC motor drives," in *2017 International Conference on Energy, Communication, Data Analytics and Soft Computing (ICECDS)*, Aug. 2017, pp. 537–540.

[13] D. Hanselman, *Brushless Permanent Magnet Motor Design*, 2nd ed. Ohio, USA: Magna Physics Publishing, 2006.

[14] L. L. Wang, J. X. Shen, P. C. K. Luk, W. Z. Fei, C. F. Wang, and H. Hao, "Development of a Magnetic-Geared Permanent-Magnet Brushless Motor," *IEEE Transactions on Magnetics*, vol. 45, no. 10, pp. 4578–4581, Oct. 2009.

[15] S. Leitner, H. Gruebler, and A. Muetze, "Innovative Low-Cost Sub-Fractional HP BLDC Claw-Pole Machine Design for Fan Applications," *IEEE Transactions on Industry Applications*, vol. 55, no. 3, pp. 2558–2568, May 2019.

[16] B. K. Lee and M. Ehsani, "Advanced bldc motor drive for low cost and high performance propulsion system in electric and hybrid vehicles," in *IEMDC 2001. IEEE International Electric Machines and Drives Conference (Cat. No.01EX485)*, June 2001, pp. 246–251.

[17] S. Dunkl, A. Muetze, and G. Schoener, "Design Constraints of Small Single-Phase Permanent Magnet Brushless DC Drives for Fan Applications," *IEEE Transactions on Industry Applications*, vol. 51, no. 4, pp. 3178–3186, July 2015.

[18] Weizi Wang, Zhigan Wu, Wanbing Jin, and Jianping Ying, "Starting methods for hall-less single phase bldc motor," in *31st Annual Conference of IEEE Industrial Electronics Society, 2005. IECON 2005.*, Nov. 2005.

[19] S. Bentouati, Z. Zhu, and D. Howe, "Permanent magnet brushless dc motors for consumer products," *IET Conference Proceedings*, pp. 118–122(4), Jan. 1999. [Online]. Available: https://digital-library.theiet.org/content/conferences/10.1049/cp_19991001

[20] L. I. Iepure, L. Tutelea, and I. Boldea, "FEM analysis and control of a tapered airgap single phase PMSM," in *2008 11th International Conference on Optimization of Electrical and Electronic Equipment*, May 2008, pp. 241–248.

[21] Hoe-Cheon Kimr, Jun-Hee Han, and Tae-Uk Jung, "Analysis of torque characteristic according to the asymmetrical airgap of the BLDC motor for cooling-fan," in *2013 International Conference on Electrical Machines and Systems (ICEMS)*, Oct. 2013, pp. 1277–1280.

[22] C. Chiu, Y. Chen, Y. Liang, and R. Liang, "Optimal Driving Efficiency Design for the Single-Phase Brushless DC Fan Motor," *IEEE Transactions on Magnetics*, vol. 46, no. 4, pp. 1123–1130, April 2010.

[23] S. Leitner, H. Gruebler, and A. Muetze, "Low-cost sub-fractional horsepower brushless direct current claw-pole machine topology for fan applications," in *2018 IEEE Applied Power Electronics Conference and Exposition (APEC)*, 2018, pp. 1242–1248.

[24] Elmos Semiconductor AG. (2017) 500mA BLDC Motor Controller–E523.81. [Accessed: Oct. 22, 2019]. [Online]. Available: https://www.elmos.com/produkte/motor-control-ics/brushless-dc-motor-controller-ic/e52381.html

[25] E. Bolte, *Elektrische Maschinen: Grundlagen Magnetfelder, Wicklungen, Asynchronmaschinen, Synchronmaschinen, Elektronisch kommutierte Gleichstrommaschinen*. Springer, 2012.

[26] H. Gruebler, F. Krall, S. Leitner, and A. Muetze, "Space Mapping-Based Fractional Horsepower Permanent Magnet Motor Design," in *2019 IEEE International Electric Machines Drives Conference (IEMDC)*, May 2019, pp. 455–460.

[27] J. R. Hendershot and T. J. E. Miller, *Design of Brushless Permanent-Magnet Machines*. Motor Design Books LLC, 2010.

[28] HBM GmbH. (2018) HBM Genesis High-Speed Data Aquisition System. [Accessed: Oct. 10, 2019]. [Online]. Available: https://www.hbm.com/en/3868/data-recorder-gen3i-and-transient-recorder/

[29] LEM Holding SA. (2015) Current Transducer IT 65-S ULTRASTAB. [Accessed: Oct. 24, 2019]. [Online]. Available: https://www.lem.com/en/it-65s-ultrastab

[30] JSOL Corporation. (2018) JMAG-Designer, FEA Software for Electromechanical Design. [Accessed: Oct. 20, 2019]. [Online]. Available: https://jmag-international.com/products/jmag-designer/index.html

[31] MathWorks. (2018) MATLAB/Simulink Product Families. [Accessed: Oct. 25, 2019]. [Online]. Available: https://www.mathworks.com/products.html

[32] Honeywell Inc., "Solid State Hall Effect Sensors," SS490 Series datasheet.

[33] M. Bali and A. Muetze, "Influences of CO2 Laser, FKL Laser, and Mechanical Cutting on the Magnetic Properties of Electrical Steel Sheets," *IEEE Transactions on Industry Applications*, vol. 51, no. 6, pp. 4446–4454, Nov. 2015.

[34] H. Naumoski, B. Riedmüller, A. Minkow, and U. Herr, "Investigation of the influence of different cutting procedures on the global and local magnetic properties of non-oriented electrical steel," *Journal of Magnetism and Magnetic Materials*, vol. 392, pp. 126 – 133, 2015.

[35] R. Siebert, J. Schneider, and E. Beyer, "Laser cutting and mechanical cutting of electrical steels and its effect on the magnetic properties," *IEEE Transactions on Magnetics*, vol. 50, no. 4, pp. 1–4, April 2014.

[36] R. Qu and T. A. Lipo, "Analysis and modeling of air-gap and zigzag leakage fluxes in a surface-mounted permanent-magnet Machine," *IEEE Transactions on Industry Applications*, vol. 40, no. 1, pp. 121–127, 2004.

[37] M. F. Momen and S. Datta, "Analysis of Flux Leakage in a Segmented Core Brushless Permanent Magnet Motor," *IEEE Transactions on Energy Conversion*, vol. 24, no. 1, pp. 77–81, March 2009.

[38] J. R. Hendershot and T. J. E. Miller, *Design of Brushless Permanent-Magnet Motors*. Magna Physics Pub. ; Clarendon Press Hillsboro, OH : Oxford, 1994.

[39] H. Yeo, D. Lim, D. Woo, J. Ro, and H. Jung, “Magnetic Equivalent Circuit Model Considering Overhang Structure of a Surface-Mounted Permanent-Magnet Motor,” *IEEE Transactions on Magnetics*, vol. 51, no. 3, pp. 1–4, Mar. 2015.

[40] H. Roters, *Electromagnetic Devices*. Wiley, 1941.

[41] TDK Corporation, “Magnetic Circuit Design Guide,” [Accessed: Jun. 11, 2019]. [Online]. Available: https://product.tdk.com/info/en/products/magnet/technote/designguide.html

[42] M. K. Meena, R. Khanna, and Dipankar, “Nonlinear Inductance Measurement Using an Energy Storage Approach,” in *2011 International Symposium on Electronic System Design*, Dec. 2011, pp. 30–33.

[43] T. Cox, F. Eastham, and J. Proverbs, “End Turn Leakage Reactance of Concentrated Modular Winding Stators,” *IEEE Transactions on Magnetics*, vol. 44, no. 11, pp. 4057–4061, Nov 2008.

[44] *Magnetische Werkstoffe - Teil 4: Verfahren zur Messung der MagnetischenEigenschaften von Weichmagnetischen Werkstoffen im Gleichfeld*, International Electrotechnical Commission (IEC) Std. 60 404-4, Rev. 2009-10, 1995.

[45] L. Michalowsky, *Magnettechnik-Grundlagen und Anwendungen*. Fachbuchverlag Leipzig-Köln, 1993.

[46] *Magnetische Werkstoffe - Teil 6: Verfahren zur Messung der magnetischen Eigenschaften weichmagnetischer und pulverförmiger Werkstoffe bei Frequenzen im Bereich 20 Hz bis 200 kHz mit Hilfe von Ringproben*, International Electrotechnical Commission (IEC) Std. 60 404-6, Rev. 2009-06, 2003.

[47] S. Tumanski, *Handbook of Magnetic Measurements*. CRC Press, 2011.

[48] H. Gruebler, F. Krall, S. Leitner, and A. Muetze, “Loss-Surface-Based Iron Loss Prediction for Fractional Horsepower Electric Motor Design,” in *2018 20th European Conference on Power Electronics and Applications (EPE'18 ECCE Europe)*, Sep. 2018, pp. P.1–P.8.

[49] M. L. G. Kissin, J. T. Boys, and G. A. Covic, “Interphase mutual inductance in polyphase inductive power transfer systems,” *IEEE Transactions on Industrial Electronics*, vol. 56, no. 7, pp. 2393–2400, July 2009.